The Astrophysical Journal, 995:41 (23pp), 2025 December 10 https://doi.org/10.3847/1538-4357/ae147c

3D Modeling of Moist Convective Inhibition in Idealized Sub-Neptune Atmospheres

Namrah Habib and Raymond T. Pierrehumbert
Atmospheric, Oceanic and Planetary Physics, Department of Physics, University of Oxford, Parks Road, OX1 3PU, Oxford, UK; namrah.habib@physics.ox.ac.uk
Received 2024 September 26; revised 2025 October 14; accepted 2025 October 15; published 2025 December 3

Abstract

Atmospheric convection behaves differently in hydrogen-rich atmospheres compared to higher mean molecular weight atmospheres due to compositional gradients of tracers. Previous 1D studies predict that when a condensable tracer exceeds a critical mixing ratio in H_2-rich atmospheres, convection is inhibited, leading to the formation of radiative layers where the temperature decreases faster with height than in convective profiles. We use 3D convection-resolving simulations to test whether convection is inhibited in H_2-rich atmospheres when the tracer mixing ratio exceeds the critical threshold, while including processes neglected in 1D, e.g., turbulent mixing and evaporation. We run two sets of simulations. First, we perform simulations initialized on saturated isothermal states and find that compositional gradients can destabilize isothermal atmospheres. Second, we perform simulations initialized on adiabatic profiles, which show distinct, stable inhibition layers form when the condensable tracer exceeds the critical threshold. Within the inhibition layer, only a small amount of energy is carried by latent heat flux, and turbulent mixing transports a small amount of tracer upward, but both are generally too weak to sustain substantial tracer or heat transport. The thermal profile gradually relaxes to a steep radiative state, but radiative relaxation timescales are long. Our results suggest stable layers driven by condensation-induced convective inhibition form in H_2-rich atmospheres, including those of sub-Neptune exoplanets.

Unified Astronomy Thesaurus concepts: Exoplanet atmospheres (487); Exoplanet atmospheric composition (2021); Atmospheric structure (2309); Planetary atmospheres (1244)

1. Introduction

Sub-Neptune exoplanets, planets with radii between ∼1.5 and 4 Earth radii, are one of the most commonly detected types of exoplanets. However, the nature and interior structure of these exoplanets is still unknown. A commonly accepted model for sub-Neptune structure is a hydrogen–helium-dominated atmosphere over a rocky or icy core (V. Van Eylen et al. 2018). However, other possible structures have been proposed and include; "water worlds" (R. Luque & E. Pallé 2022), which have high volatile fraction envelops, hot supercritical atmospheres containing a mixture of H_2 and H_2O (R. T. Pierrehumbert 2023; B. Benneke et al. 2024), and "Hycean worlds" (N. Madhusudhan et al. 2021), planets with shallow hydrogen–helium-dominated atmospheres overlaying a water-rich interior and large oceans. Understanding the atmospheric state and dynamics of hydrogen-rich atmospheres is crucial to our understanding of sub-Neptune exoplanets. In this work, we explore vertical mixing and the temperature structure of H_2-rich atmospheres to inform our understanding of sub-Neptunes and other planets with H_2-dominated atmospheres.

In H_2-dominated atmospheres, vertical mixing due to convection behaves differently compared to higher mean molecular weight atmospheres, like that of Earth. Any atmospheric tracer will have a higher mean molecular weight than the background atmosphere in H_2-rich atmospheres. Therefore, a parcel of pure H_2 will be less dense and more buoyant than a parcel containing a mixture of H_2 with any atmospheric tracer at the same temperature and pressure. Tracers in H_2-dominated atmospheres can strongly stabilize (N. Habib & R. T. Pierrehumbert 2024) and potentially inhibit convection (T. Guillot 1995; A. J. Friedson & E. J. Gonzales 2017; J. Leconte et al. 2017). N. Habib & R. T. Pierrehumbert (2024) demonstrated through 3D convection-resolving simulations that compositional gradients of noncondensing tracers (i.e., dry convection) significantly stabilize and affect the atmospheric temperature state in H_2-dominated atmospheres.

In moist convection, the atmospheric tracer is near saturation and condenses in some part of the temperature–pressure range within the atmosphere, releasing latent heat that further drives vertical mixing and impacts the temperature profile. The effects of compositional gradients on moist convection (i.e., moist compositional convection) in H_2-dominated atmospheres has primarily been explored using 1D analytical studies (T. Guillot 1995; C. Li & A. P. Ingersoll 2015; A. J. Friedson & E. J. Gonzales 2017; J. Leconte et al. 2017). Notably, T. Guillot (1995) found that vertical mixing due to moist convection is suppressed when the abundance of an atmospheric tracer exceeds a critical threshold in saturated, H_2-dominated atmospheres.

Following standard meteorological definition, convective inhibition or shutdown refers to the suppression of buoyancy, thus preventing vertical mixing and the initiation of convection (K. A. Emanuel 1994). T. Guillot (1995) argued that in H_2 atmospheres, when convection is inhibited by the gradient of a condensing tracer, heat can only be transferred by radiation or conduction.

J. Leconte et al. (2017), and A. J. Friedson & E. J. Gonzales (2017) extended the theory of condensation-driven convective inhibition to hypothesize that compositional gradients in H_2-rich atmospheres could stabilize the atmosphere against all vertical mixing in the 1D regime, including double diffusive convection.

J. Leconte et al. (2017) and A. J. Friedson & E. J. Gonzales (2017) proposed radiation as the primary mechanism to transport heat though condensation-driven stable regions within the atmosphere. Furthermore, J. Leconte et al. (2017) argued that in regions where the abundance of a saturated tracer exceeds the critical threshold defined by T. Guillot (1995), a radiative layer forms where the temperature profile is

superadiabatic. In superadiabatic regions, temperature decreases with height faster than it would in a convective layer. Radiative layers imply that the deep internal temperature in H_2-dominated atmospheres is much hotter than it would be under a purely convective atmospheric profile, assuming the temperature at the top of the atmosphere is the same.

J. Leconte et al. (2017) suggested the structure of H_2-rich atmospheres consists of a deep dry convective region, overlaid by a radiative superadiabatic region, and topped by a condensing, moist convective region. Several recent studies have applied the hypothesis that superadiabatic layers form due to condensation-driven convective inhibition in H_2-rich atmospheres, focusing on Hycean worlds (H. Innes et al. 2023) and magma-ocean planets (S. Markham et al. 2022; W. Misener & H. E. Schlichting 2022). However, determining whether condensation-driven convective inhibition occurs requires 3D models, as 1D theory relies on assumptions that may not be valid in more realistic atmospheric settings.

In this work, we test the hypotheses proposed by T. Guillot (1995), which suggests that convection is suppressed when a saturated condensing tracer exceeds a critical threshold. 1D radiative-convective models allow for fast exploration of planetary structure but often make assumptions that may not be justified in realistic settings. In particular, 1D radiative-convective models typically neglect subsaturation of the condensable tracer, evaporation of condensates, and turbulent mixing. We aim to explore the robustness of condensation-driven convective inhibition in H_2-rich atmospheres while accounting for the processes that are neglected in 1D radiative-convective models.

In this work, we adopt the standard meteorological definition of convective inhibition: the suppression of buoyancy and consequently convective-driven vertical mixing (K. A. Emanuel 1994). Using 3D convection-permitting simulations with Cloud Model 1 v20.3 (CM1; G. H. Bryan 2021), we explore the vertical temperature and compositional structure in H_2-dominated atmospheres when a saturated water vapor tracer exceeds the critical threshold defined by T. Guillot (1995). Our objectives are to answer the following questions:

1. Is convection inhibited when the tracer abundance is greater than the critical threshold defined by T. Guillot (1995)?
2. If convective inhibition regions form, is the temperature profile in these regions superadiabatic?
3. How are heat and moisture transport impacted if convection is inhibited?

The aim of this work is to understand how condensation-driven convective inhibition is affected by processes neglected in 1D models including turbulent mixing, evaporation of condensates, and subsaturation. We focus on the suppression and stability of vertical mixing due to convection as a local effect, and leave studying compositional suppression of double diffusive convection (e.g., A. J. Friedson & E. J. Gonzales 2017; J. Leconte et al. 2017) and global effects of condensation-driven convective inhibition to future work (e.g., T. Guillot et al. 2022).

Recently, J. Leconte et al. (2024) used 3D convection-permitting simulations to explore the formation of convectively stable regions when tracer abundance exceeds a critical threshold for the sub-Neptune K2 18 b. Their results suggest the development of convectively stable regions, and reproduced the atmospheric structure proposed by J. Leconte et al. (2017), where a moist convective layer overlies a radiative superadiabatic region, on top of a dry convection layer. However, J. Leconte et al. (2024) also found the condensable tracer can be transported through convectively stable regions via turbulent mixing, highlighting the importance of 3D studies. We compare our simulation results with those presented by J. Leconte et al. (2024) in Section 4.

In Section 2 we review the condensing compositional convection stability criterion. In Section 3 we describe our CM1 simulation setup, and we present our simulation results and discussions in Section 4.

2. Theoretical Background

Atmospheric convection is defined as the vertical mixing due to a steady gravitational field acting upon vertical variations in density (i.e., buoyancy; K. A. Emanuel 1994). Typically, in an atmosphere, perturbations in density are either due to temperature or compositional variations. Convective inhibition is defined as the suppression of positive buoyancy and vertical mixing (K. A. Emanuel 1994). In this work, we test whether condensing tracers can inhibit convection in H_2-rich atmospheres.

The effects of atmospheric tracers on convection (also called virtual effects) are typically represented using virtual temperature

$$T_v = T\left(\frac{1 + q_v/\epsilon}{1 + q_v}\right), \tag{1}$$

where T is the atmospheric temperature (K), q_v is the vapor mixing ratio of the atmospheric tracer ($\mathrm{kg\,kg^{-1}}$), and $\epsilon = M_v/M_b$ is the ratio of the mean molecular weight of the tracer to the background atmosphere (K. A. Emanuel 1994). The subscript b refers to the background atmosphere bulk composition gas, while the tracer, is denoted by subscript v (for "vapor"). Effectively, T_v represents density in units of temperature and allows us to write the ideal gas law as $p = \rho R_b T_v$, where p is the total atmospheric pressure, R_b is the gas constant for the background atmosphere, and ρ is the total atmospheric density. The vapor mixing ratio, q_v, quantifies how much atmospheric tracer is present relative to the background air and is defined as the ratio of the density of the tracer (ρ_v) relative to the background atmosphere density (ρ_b)

$$q_v = \rho_v/\rho_b. \tag{2}$$

Compositional effects on convection are determined by how much tracer is present and ϵ. If the atmospheric tracer has a lower mean molecular weight than the bulk atmosphere, then $\epsilon < 1$ and $T_v > T$, and the atmospheric tracer can *enhance* buoyancy relative to a parcel of pure background atmosphere at the same temperature. Conversely, when the atmospheric tracer is heavier than the background atmosphere, $\epsilon > 1$, and the presence of tracers can *suppress* convection. For H_2-rich atmospheres with a water vapor tracer, $\epsilon = 8.9$, while for water vapor in Earth's atmosphere, $\epsilon = 0.6$.

When the tracer does not condense, stability against convection can be approximated by

$$\frac{d\ln T_{v,\mathrm{amb}}}{d\ln p} \leqslant \beta_{\mathrm{mix}}, \tag{3}$$

where $T_{v,\mathrm{amb}}$ is the virtual temperature profile of the ambient atmosphere, p is the atmospheric pressure, and $\beta_{\mathrm{mix}} \equiv \frac{R_{\mathrm{mix}}}{c_{p,\mathrm{mix}}}$ where R_{mix} and $c_{p,\mathrm{mix}}$ are a representative specific gas constant and heat capacity, respectively, at constant pressure, respectively, for the mixture of tracer with the background atmosphere. Equation (3) is a form of the Ledoux criterion for local stability (P. Ledoux 1947) and describes the stability against infinitesimal displacements of a parcel containing a mixture of the bulk atmosphere and a noncondensing tracer (e.g., N. Habib & R. T. Pierrehumbert 2024).

To derive the condensing convective stability criterion, we must quantify how condensation affects the composition profiles of both the background atmosphere and the rising air parcel. When the atmospheric tracer condenses, a key difference from the noncondensing case is that the vapor mixing ratio is constrained by temperature via the saturation vapor pressure. Assuming the condensed liquid phase is denser than the vapor phase, the Clausius–Clapeyron relation gives the saturation vapor pressure as

$$\frac{d\ln e_{\mathrm{sat}}}{d\ln T} = \frac{L_v}{R_v T}, \tag{4}$$

where e_{sat} is the saturation vapor pressure of the condensable tracer at a given temperature T, L_v is the latent heat of vaporization, and R_v is the gas constant of the condensable tracer. For a given temperature, the saturated vapor mixing ratio is

$$q_{v,\mathrm{sat}} = \epsilon\left(\frac{e_{\mathrm{sat}}}{p - e_{\mathrm{sat}}}\right). \tag{5}$$

Saturation at a given (p, T) is determined using the relative humidity, RH, which compares the partial pressure of the tracer to its saturation vapor pressure

$$\mathrm{RH} = \frac{p_v}{e_{\mathrm{sat}}} = \left(\frac{q_v}{\epsilon + q_v}\right)\left(\frac{p}{e_{\mathrm{sat}}}\right), \tag{6}$$

where p_v is the partial pressure of the tracer at (p, T).

Assuming a saturated air parcel is displaced approximately adiabatically without any mixing with its surroundings, the temperature profile of the rising parcel is given by

$$\frac{d\ln T^*_{\mathrm{ad}}}{d\ln p} = \beta_{\mathrm{mix}}\left[\frac{1 + q_{v,\mathrm{sat}}\left(\frac{L_v}{R_b T}\right)}{1 + q_{v,\mathrm{sat}}\left(\frac{L_v}{c_{p,\mathrm{mix}}T}\right)\left(\frac{L_v}{R_v T}\right)\left(\frac{1+q_{v,\mathrm{sat}}/\epsilon}{1+q_{v,\mathrm{sat}}}\right)}\right]. \tag{7}$$

Equation (7) is the moist adiabat and gives the temperature–pressure profile of a saturated air parcel as it is displaced (K. A. Emanuel 1994). Equation (7) assumes that the volume of the condensed phase is negligible compared to the vapor phase of the atmospheric tracer, and all condensed phases are instantaneously removed. We do not consider the compositional gradient of condensed phases in determining atmospheric stability in this work.

To determine convective stability considering compositional gradients of a condensing tracer, we need to assess how condensation affects the mean molecular weight gradient of both the displaced air parcel and the background atmosphere. As a saturated air parcel is displaced, condensation leads to a change in the composition of the parcel. Additionally, the background saturated atmosphere exhibits a compositional gradient because the vapor mixing ratio changes with altitude, following the saturation vapor pressure curve. The compositional gradient is given by

$$\frac{d\ln\mu}{d\ln p} = q_{v,\mathrm{sat}}\left(\frac{1 - 1/\epsilon}{1 + q_{v,\mathrm{sat}}}\right)\left[\left(\frac{L_v}{R_v T}\right)\left(\frac{d\ln T}{d\ln p}\right) - 1\right], \tag{8}$$

where μ is the total mean molecular weight of the atmosphere (T. Guillot 1995; J. Leconte et al. 2017).

Stability to convection can be determined by comparing the density, or virtual temperature, of a displaced saturated air parcel to that of the surrounding saturated atmosphere. To compare the virtual temperature directly, we would need to solve Equations (8) and (7) and account for the change in the composition of the displaced air parcel due to condensation. Alternatively, we consider stability against infinitesimal displacements and compare the gradient of virtual temperature of a saturated parcel to that of the ambient saturated atmosphere where $\frac{d\ln T_v}{d\ln p} = \frac{d\ln T}{d\ln p} - \frac{d\ln\mu}{d\ln p}$. A saturated parcel is stable against infinitesimal displacements when

$$\left(\frac{d\ln T}{d\ln p} - \frac{d\ln\mu}{d\ln p}\right)\Bigg|_{\mathrm{amb}} - \left(\frac{d\ln T}{d\ln p} - \frac{d\ln\mu}{d\ln p}\right)\Bigg|_{\mathrm{parcel}} \leqslant 0 \tag{9}$$

where $\left(\frac{d\ln T}{d\ln p}\right)\Big|_{\mathrm{parcel}} = \frac{d\ln T^*_{\mathrm{ad}}}{d\ln p}$ is the temperature gradient of the saturated parcel given by the moist adiabat (Equation (7)), and $\left(\frac{d\ln T}{d\ln p}\right)\Big|_{\mathrm{amb}}$ is the temperature gradient of the background atmosphere. $\frac{d\ln\mu}{d\ln p}$ is given by Equation (8) and can be evaluated for the parcel and ambient atmosphere using $\frac{d\ln T^*_{\mathrm{ad}}}{d\ln p}$ and $\left(\frac{d\ln T}{d\ln p}\right)\Big|_{\mathrm{amb}}$, respectively.

Simplifying Equation (9) using Equation (8) yields

$$(\nabla_{\mathrm{amb}} - \nabla^*_{\mathrm{ad}})\left(1 - \left(\frac{q_{v,\mathrm{sat}}}{1 + q_{v,\mathrm{sat}}}\right)(1 - 1/\epsilon)\left(\frac{L_v}{R_v T}\right)\right) \leqslant 0, \tag{10}$$

where $\nabla = \frac{d\ln T_x}{d\ln p}$, "amb" represents the atmospheric temperature gradient, and the "*ad" represents the temperature gradient defined by the moist adiabat. Equation (10) is the Guillot criterion for local stability against condensing compositional convection (T. Guillot 1995).

When the atmospheric tracer is lighter than the background atmosphere so that $\epsilon < 1$, the mean molecular weight term, $(1 - 1/\epsilon)$, will always be negative, meaning that the compositional term in Equation (10) (second bracket) is always positive. Therefore, in the $\epsilon < 1$ case, convection occurs when $\nabla_{\mathrm{amb}} > \nabla^*_{\mathrm{ad}}$.

Conversely, when $\epsilon > 1$, a compositional gradient can stabilize an unstable atmospheric temperature. Consider $\nabla_{\mathrm{amb}} > \nabla^*_{\mathrm{ad}}$: in the absence of a compositional gradient, the ambient temperature profile is unstable, and convection will occur. However, when accounting for the compositional effects, the compositional gradient can stabilize an unstable atmosphere to infinitesimal displacements and inhibit

Table 1
Atmospheric Constants Used within the CM1 Condensing Compositional Convection Simulations

	c_p (J kg^{-1} K^{-1})	c_v (J kg^{-1} K^{-1})	R (J kg^{-1} K^{-1})	$\varepsilon = M_v/M_b$	κ (m^2 kg^{-1})
Hydrogen (Background atmosphere)	14304.0	10160.0	4144.0	8.94	1.18×10^{-4}
Water Vapor (Condensing tracer)	1870.0	1408.5	461.5	N/A	0.01

convection when $q_{v,\mathrm{sat}} \geqslant q_{\mathrm{crit}}$ where

$$q_{\mathrm{crit}} = \frac{R_v T}{L_v(1 - 1/\epsilon) - R_v T} \tag{11}$$

(T. Guillot 1995). Compositional gradients of condensable tracers in H_2-dominated atmospheres can provide a strong stabilizing mean molecular weight gradient that can inhibit convection when $q_v \geqslant q_{\mathrm{crit}}$.

In this work, we use 3D convection-permitting simulations to explore the atmospheric structure when accounting for compositional gradients of condensing tracers in H_2-dominated atmospheres. 3D convection-permitting simulations allow us to build upon the theory presented in this section by additionally considering the effects of turbulent mixing, subsaturation, and evaporation on the atmospheric temperature profile and stable layers. Turbulent mixing is defined as random chaotic turbulent motion that transports heat and mass but is not always representative of the bulk fluid motion. Turbulent mixing differs from convective mixing because convection is buoyancy-driven bulk fluid movement.

3. Methods

We use CM1 (G. H. Bryan 2021) to perform idealized simulations of condensing compositional convection. CM1 is a nonhydrostatic convection-resolving model that has been extensively used to study atmospheric flows. In this work, we utilize CM1 version 20.3 from N. Habib & R. T. Pierrehumbert (2024), which incorporates modifications to the original code that include setting the thermodynamic constants and planetary parameters using an input file, and revising the buoyancy equation to account for nondilute concentrations of atmospheric tracers. An overview of the CM1 equations is provided in Appendix B, and a detailed description of the model is presented by G. H. Bryan (2021) and G. H. Bryan & H. Morrison (2012) .

The thermodynamic constants used in this study are listed in Table 1. Gravity is set to 9.8 m s^{-2} in all simulations. CM1 is run using the fully compressible equations in Large-Eddy Simulation (LES) mode. Sub-grid scale turbulent mixing is included using a turbulent kinetic energy (TKE) closure (J. W. Deardorff 1980) to parameterize turbulent mixing at unresolved scales similar to previous studies (e.g., X. Tan et al. 2021; M. Lefèvre et al. 2022; N. Habib & R. T. Pierrehumbert 2024). The TKE scheme in CM1 is adapted to the user-imputed thermodynamic constants.

We use a rigid bottom boundary condition with a fixed surface temperature, and horizontal periodic boundary conditions. The turbulent heat and momentum exchange at the bottom boundary is calculated using the original CM1 formulation. Additionally, a Rayleigh damping layer is applied in the top 10 km of the domain to damp out any upward propagating gravity waves. The time step is set to 3 s, and radiative calculations are run once per minute.

We use the R. Rotunno & K. A. Emanuel (1987) condensation scheme to account for condensation of the water vapor tracer, rainout, and evaporation. The Rotunno and Emanuel scheme only considers the vapor and liquid phases, where the vapor mixing ratio is, $q_v = \frac{\rho_v}{\rho_b}$, and the liquid condensate mixing ratio is $q_l = \frac{\rho_l}{\rho_b}$. ρ_l is the density of liquid condensate, ρ_b is the background atmosphere density, and ρ_v is the density of the atmospheric tracer in vapor form. In the Rotunno and Emanuel scheme, a distinction is made between *cloud* and *rain* water. Condensate with $q_l \leqslant 1$ g kg^{-1} is cloud condensate and has a terminal fall velocity of $V = 0$ m s^{-1}, while condensates with $q_l > 1$ g kg^{-1} is rain condensate and has a terminal fall velocity of $V = -10$ m s^{-1}.

Condensation is modeled as a two-step process. First, precipitation occurs in situ, and second, the condensate is removed by rainout if $V < 0$. Condensation occurs at a given time step when $q_v(p) > q_{v,\mathrm{sat}}(p)$, where $q_{v,\mathrm{sat}}(p)$ is the saturation vapor mixing ratio at the given (T, p). Condensation occurs to remove excess water vapor relative to saturation such that after condensation $q_v(p) = q_{v,\mathrm{sat}}(p)$. When condensation occurs, a small amount of liquid condensate forms, the vapor pressure of the tracer is adjusted to the saturation vapor pressure, and the latent heat release of condensation causes the local temperature to increase slightly.

Rainout moves condensates to lower atmospheric layers, where they evaporate if the layers are subsaturated. Condensates evaporate in a grid cell if $q_v(p) < q_{v,\mathrm{sat}}(p)$ and $q_l > 0$. Evaporation occurs until the condensate is depleted or the layer reaches saturation, $q_v(p) = q_{v,\mathrm{sat}}(p)$, depending on which occurs first. If a layer is saturated or reaches saturation before the condensate is depleted, the condensate that remains is passed to the next lower layer, and the process repeats layer by layer to the surface. When evaporation occurs, the temperature decreases slightly due to the latent heat required to evaporate the liquid, and the vapor pressure of the tracer is again adjusted accordingly. Detailed cloud condensation growth or microphysics are not considered.

The TWOSTR (A. Kylling et al. 1995) numerical package is used to solve the gray gas radiative transfer equations. TWOSTR is a two-stream plane-parallel gray gas radiative transfer model. A constant background opacity and a constant water vapor opacity are set to $\kappa_b = 1.18 \times 10^{-4}$ m^2 kg^{-1} and $\kappa_v = 0.01$ m^2 kg^{-1}, respectively, based on previous studies (K. Menou 2011; R. S. Freedman et al. 2014; H. Innes et al. 2023). The total opacity κ varies as a function of pressure p and is given by

$$\kappa(p) = \frac{\kappa_b + \kappa_v * q_v(p)}{1 + q_v}, \tag{12}$$

where q_v is the vapor mixing ratio of the atmospheric tracer, and κ_b and κ_v are the opacity of the background air and atmospheric tracer, respectively. Shortwave heating of the upper atmosphere and scattering are neglected. Additionally, we do not set a distinct cloud opacity and do not consider cloud-radiative feedbacks.

Table 2
Initial Atmospheric Sounding Parameters and Domain Size Used for the CM1 Condensing Compositional Convection Simulations

		p_s (bar)	T_s (K)	$q_{v,s}$ (kg kg^{-1})	$q_{\rm crit}$ (kg kg^{-1})	L_x (km)	L_z (km)	nx	nz	Time (days)
				Initial Isothermal Simulations						
(a)	No Radiation and $q_v \approx q_{\rm crit}$	1	273	0.055	0.057	1152	350	192	70	100
(b)	$q_v \approx q_{\rm crit}$	1	273	0.055	0.057	1152	350	192	70	100
(c)	$q_v > q_{\rm crit}$	1	300	0.321	0.062	1152	150	192	30	100
(d)	$q_v < q_{\rm crit}$	20	300	0.016	0.062	1152	520	192	104	100
				Initial Adiabatic Simulations						
(a)	Dry then Moist Adiabat	1	450	0.2	0.1	1200	500	192	250	1750
(b)	Moist Adiabat	1	300	0.2	0.1	1200	400	192	200	600
(c)	Superadiabatic	1	315	0.8	0.1	384	200	192	200	600

Note. Note, L_x and L_z are the horizontal domain width and vertical domain height, respectively. The horizontal domain is a square such that $L_x = L_y$, and the horizontal resolution is the same in the x- and y-directions. Simulations are listed with alphabetical identifiers that correspond to later plots. Note that isothermal simulations and adiabatic simulations are plotted separately.

The radiation setup differs from sub-Neptune exoplanets, where the atmosphere is largely heated by in situ shortwave absorption. We opted for a simplified setup where convection can occur, allowing us to capture the effects of radiation on the temperature profile without the complexity and computational demand of a more realistic radiative transfer scheme. The CM1 setup represents a sub-Neptune with a deep interior containing water vapor without a condensed ocean at the bottom.

We perform three sets of condensing compositional convection simulations in this work:

1. *Isothermal Simulations*. CM1 is initialized in a saturated isothermal atmospheric state. Without compositional effects, isothermal atmospheres are stable to convection. Destabilization of isothermal layers is an important novel feature.
2. *Adiabatic Simulations*. CM1 is initialized on adiabatic temperature profiles to explore if layer(s) of convective inhibition form where $q_{v,\rm sat} \geqslant q_{\rm crit}$ and how this impacts the temperature and compositional profile.
3. *Superadiabatic Simulations*. CM1 is initialized on a saturated superadiabatic temperature profile to determine if saturated superadiabatic states are stable over time when $q_{v,\rm sat} \geqslant q_{\rm crit}$.

The CM1 setup for the isothermal, adiabatic, and superadiabatic simulations are summarized in Table 2.

3.1. Isothermal Simulations

We performed a set of four isothermal simulations. All simulations were initialized with the assumption that the atmosphere is saturated throughout. Given that the initial temperature is constant across the domain, a saturated isothermal profile implies an increase in the vapor mixing ratio as pressure decreases. This effect is mathematically represented in Equation (5). Here, if T is constant, then $e_{\rm sat}$ remains constant, and as pressure decreases, $q_{v,\rm sat}$ increases. However, increasing $q_{v,\rm sat}$ indefinitely eventually causes CM1 to become numerically unstable, as it introduces more dense fluid above lighter fluid, creating a strongly unstable initial condition. Having a large amount of dense fluid at the top of the domain leads to rapid initial convective mixing with large velocities that cause the model to go unstable. Therefore, we set an arbitrary cutoff for the top of the atmosphere in these simulations to be at the point where $q_{v,\rm sat} = 1$, corresponding to 50% water by mass. This definition means that the simulation domain height depends on the isothermal temperature we set for the atmosphere.

For all of our saturated isothermal cases, the initial atmospheric state is unstable to noncondensing compositional convection by the Ledoux criterion. This is because $q_v(p)$ is increasing with height, the temperature is constant, and the tracer is denser than the background air; therefore, a denser fluid is resting above a lighter fluid. Further, atmospheric stability against moist compositional convection can be determined by considering the Guillot criterion given by Equation (10). In the case of an isothermal atmosphere, $(\nabla_{\rm amb} - \nabla^*_{\rm ad}) < 0$. Therefore, the initial atmospheric state is locally stable against convection by the Guillot criterion when $q_v(p) \leqslant q_{\rm crit}$ and unstable when $q_v(p) > q_{\rm crit}$.

We perform three saturated isothermal test cases where we set the atmospheric temperature such that the surface saturated vapor mixing ratio, $q_{v,\rm sat}(p_s)$, is approximately equal to, greater than, and less than the surface critical vapor mixing ratio $q_{\rm crit}(T_s)$ given by Equation (11). Specifically, we run simulations at

1. $T = 273$ K, $p_s = 1$ bar, and $q_{v,\rm sat}(p_s) \approx q_{\rm crit}(T_s)$.
2. $T = 300$ K, $p_s = 1$ bar, and $q_{v,\rm sat}(p_s) > q_{\rm crit}(T_s)$,
3. $T = 300$ K, $p_s = 20$ bar, and $q_{v,\rm sat}(p_s) < q_{\rm crit}(T_s)$.

We also run the 273 K test case without radiation as a control test case, where the final state is solely representative of condensing compositional convection. For the case where $q_{v,\rm sat}(p_s) < q_{\rm crit}(T_s)$, the surface pressure was adjusted to maintain the atmospheric temperature in a regime where condensation occurs while ensuring that the initial condition $q_{v,\rm sat}(p_s) < q_{\rm crit}(T_s)$ was met.

In the $q_{v,\rm sat}(p_s) > q_{\rm crit}$ simulation, the initial atmospheric state is unstable to both moist and dry compositional convection. Conversely, in the $q_{v,\rm sat}(p_s) < q_{\rm crit}$ case, the initial atmospheric state is locally stable to condensing compositional convection by the Guillot criterion in the region where $q_{v,\rm sat}(p_s) < q_{\rm crit}$ and unstable to dry compositional convection by the Ledoux criterion. In the $q_{v,\rm sat}(p_s) < q_{\rm crit}$ case, we are testing if condensation can stabilize the Ledoux unstable atmospheric state. The initial conditions were chosen to

highlight the compositional destabilization and the nature of evolution toward an end state. The domain size, resolution, and simulation time for the CM1 test cases are given in Table 2.

Recent studies report deep, radiative isothermal layers in magma-ocean planets (e.g., H. Nicholls et al. 2025) and in pure-steam atmospheres (e.g., F. Selsis et al. 2023). Here we examine the stability of isothermal layers to compositional gradients. If outgassing from a liquid-water or magma ocean allows for the buildup of condensables in the deep atmosphere, can the resulting mean molecular weight stratification maintain these isothermal layers over time? In the absence of compositional effects, an isothermal profile is statically stable to convection ($(\nabla_{\rm isothermal} - \nabla^*_{\rm ad}) < 0$). Using CM1, we explore how compositional gradients affect isothermal layers. We expect compositional gradients to destabilize isothermal layers due to the Ledoux criterion. However, in the $q_{v,\rm sat}(p_s) < q_{\rm crit}$, the initial state is stable to condensing compositional convection. The $q_{v,\rm sat}(p_s) < q_{\rm crit}$ simulation will test whether condensation can stabilize the Ledoux unstable stratification and preserve deep isothermal layers.

3.2. Adiabatic Simulations

We performed two adiabatic condensing compositional convection simulations, which were initialized: (1) with the entire atmosphere set to a moist adiabat defined by Equation (7), and (2) with the lower atmosphere following a dry adiabat with a constant $q_v = 0.2\,\mathrm{kg\,kg^{-1}}$ until the point of saturation, after which the temperature profile transitions to a moist adiabat. When the temperature in the upper atmosphere reached 150 K, the temperature profile was set to be isothermal, emulating a radiative stratosphere. The dry adiabat describes the temperature profile of an atmosphere that is well-mixed with a tracer that is either subsaturated or noncondensing in the temperature–pressure range of the atmosphere. The dry adiabat is defined as

$$\frac{d\ln T_{\rm ad}}{d\ln p} = -\frac{\boldsymbol{R}_{\rm mix}}{\boldsymbol{c_{p,\rm mix}}}, \tag{13}$$

where $R_{\rm mix}$ and $c_{p,\rm mix}$ are the specific gas constant and heat capacity at constant pressure, respectively, for the well-mixed region. The CM1 test case initialized on a dry then moist adiabat is qualitatively a sub-Neptune model with a subsaturated noncondensing convective deep atmosphere, which becomes saturated and condensing in the colder upper atmosphere. The moisture reservoir is the subsaturated deep layer, rather than a liquid ocean. Both adiabatic simulations are initialized such that $q_{v,s} > q_{\rm crit}(T_s)$.

With the adiabatic simulations, we aim to determine whether a superadiabatic temperature profile will form where $q_{v,s} > q_{\rm crit}(T_s)$ and convection is inhibited by the Guillot criterion. The domain size, resolution, and simulation duration for the CM1 test cases are summarized in Table 2.

3.3. Superadiabatic Simulation

Lastly, we perform a single simulation that is initialized on a saturated superadiabatic temperature profile defined by

$$T = T_s\left(\frac{1 + e^{-z/H}}{2}\right)^{1/4}, \tag{14}$$

where T_s is the surface temperature set to 315 K, z is the domain height, and H is a reference vertical scale height that was set to 26 km. The temperature profile was set such that the initial state is superadiabatic, the temperature decreases faster with height compared to an adiabatic profile, in the lower atmosphere. The initial tracer mixing ratio was set such that the atmosphere is fully saturated in the lower domain. In the upper atmosphere, where the temperature profile becomes isothermal, the vapor mixing ratio was set to zero in order to avoid the case where the mixing ratio is increasing with height in the isothermal region. With the superadiabatic simulation, we aim to determine if saturated superadiabatic layers remain stable over time, as predicted by the Guillot criterion. In Figure 13 shown in Appendix C, we provide the results of a CM1 simulation initialized on the same superadiabatic profile given by Equation (14), but without any condensation and moisture (dry) to benchmark that the model does evolve to a dry adiabat in the absence of condensation.

4. Results and Discussion

4.1. Initially Isothermal Simulations

Figure 1 shows the results from the four isothermal CM1 simulations in each respective row. In each row, the figure shows profiles of (from left to right) temperature (K), virtual potential temperature (K), vapor mixing ratio ($\mathrm{kg\,kg^{-1}}$), relative humidity, and condensate mixing ratio ($\mathrm{g\,kg^{-1}}$). In the first three panels, the blue line shows the initial state of the simulation, and the black line shows the final state. In the temperature panel, the gray dotted–dashed line plots a temperature profile calculated in pure radiative equilibrium, the gray dashed line is the dry adiabat defined by Equation (13), and the gray solid line plots a moist adiabat defined by Equation (7). Pure radiative equilibrium is calculated assuming a gray gas atmosphere using

$$\frac{d\ln T_{\rm RE}}{d\ln p} = -\frac{1}{4}\frac{1}{(1 + \tau_\infty - \tau)}p\frac{d\tau}{dp}, \tag{15}$$

where $T_{\rm RE}(p)$ is the temperature profile in radiative equilibrium, p is the atmospheric pressure, τ is optical depth, and τ_∞ is the total optical depth of the atmosphere (see R. T. Pierrehumbert 2010). The optical depth is related to the atmospheric opacity, κ, by $d\tau/dp = -1/(2g)\kappa(p)$, where the opacity is determined using Equation (12) with the final state CM1 vapor mixing ratio profile. In the vapor mixing ratio panel, the black dashed line plots the critical vapor mixing ratio calculated using Equation (11) of the final atmospheric state. The pressure, temperature, and vapor mixing ratio values are calculated by taking the horizontal average of the CM1 data at the given time step. The relative humidity is calculated using the 3D temperature, pressure, and vapor mixing ratio outputs from CM1, and the horizontal average of the relative humidity is shown. To complement the $T(p)$ and temperature difference panels in Figure 1, we provide a plot of the lapse rates in the isothermal simulations in Figure 14 in Appendix D.

The isothermal CM1 simulations are used to initialize the system without biasing the end state after convective mixing to be adiabatic. Isothermal profiles are typically stable to convection. However, in our simulation setup, the initial state

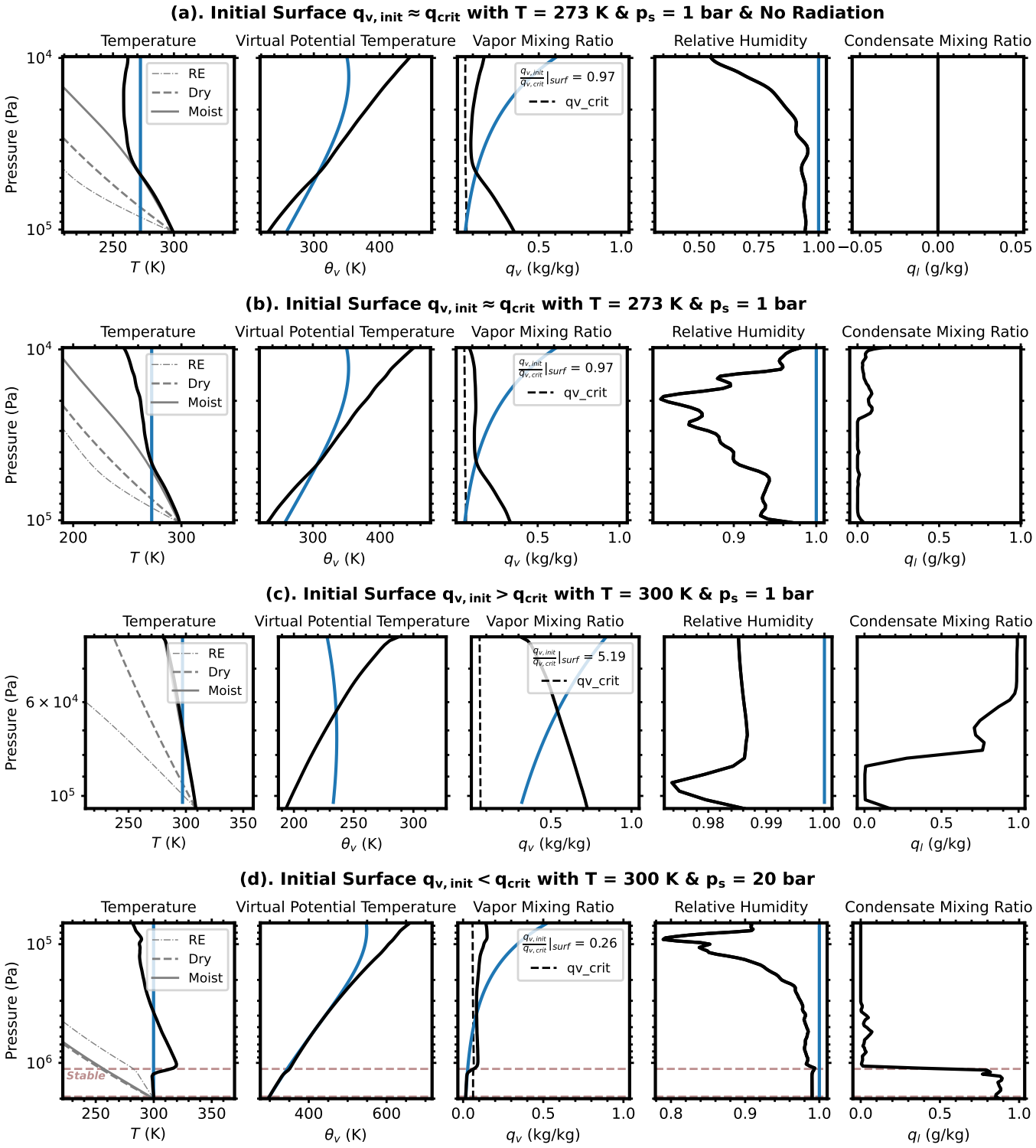

Figure 1. Overview of the atmospheric state from the initially isothermal simulations. In each row, the panels show from left to right, profiles of temperature (K), virtual potential temperature (K), vapor mixing ratio (kg kg^{-1}), relative humidity, and condensate mixing ratio (g kg^{-1}). In the temperature panels, the gray dashed and solid lines plot dry and moist adiabats, and the gray dotted–dashed line plots the temperature profile assuming gray gas pure radiative equilibrium. The dashed gray line in the vapor mixing ratio panels plots the critical vapor mixing ratio of the final state. Blue lines show the initial state, while black lines show the final state. In the third row, the final state in the temperature profile lies perfectly on top of the gray moist adiabat curve throughout the domain. The ratio $q_{v,\mathrm{init}}/q_{v,\mathrm{crit}}$ is calculated using the surface values of the initial state of the respective simulation. No initial state is shown in the q_l panels, as this was set to be zero everywhere in all of the simulations.

compositional gradient is increasing with altitude, as seen by the blue line in the q_v panels in Figure 1. Therefore, in the upper portion of the domain, the initial state is unstable to noncondensing convection, which is shown by the decreasing θ_v in the upper portion of the domain, as shown by the blue line the virtual potential temperature panels in Figure 1. Decreasing virtual potential temperature indicates convective instability. Initially, convection is driven by the Ledoux criterion, where

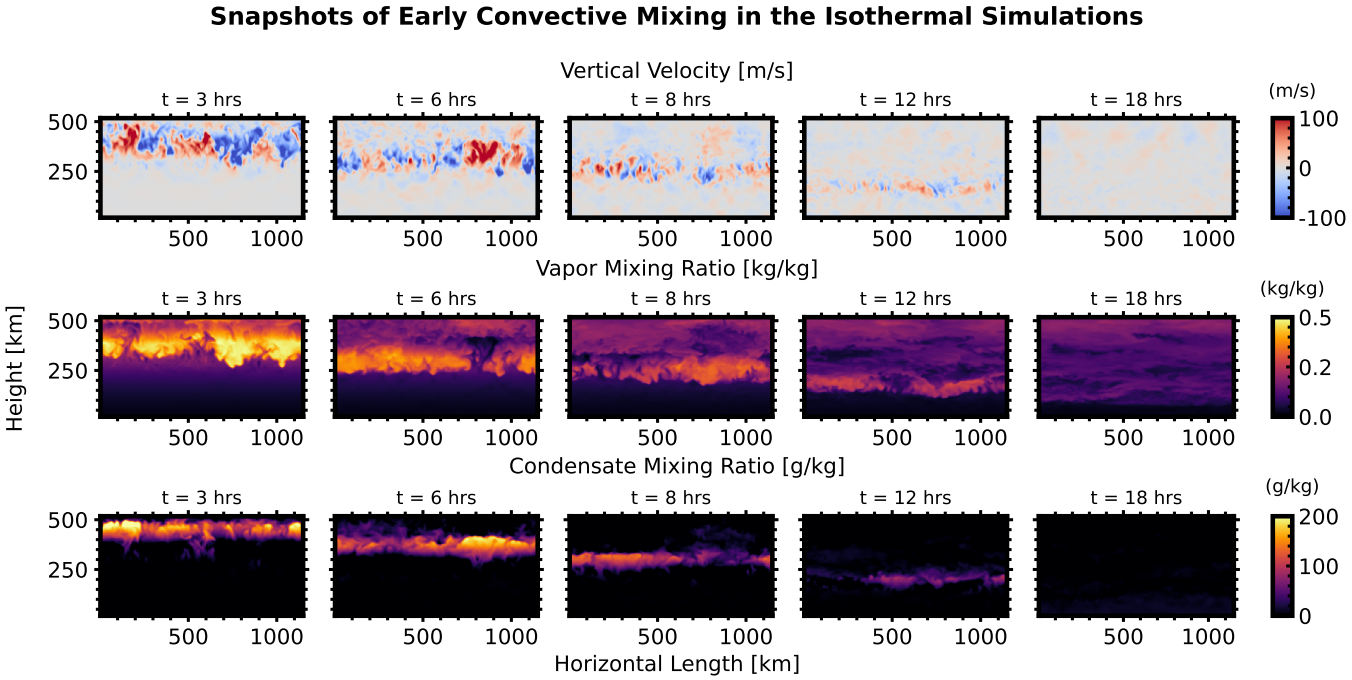

Figure 2. Snapshots of vertical velocity (top row), vapor mixing ratio (middle row), and condensate mixing ratio (bottom row) during the early rapid convective mixing phase in the isothermal simulations. All four isothermal simulations undergo a similar rapid convective mixing phase within the first 12–15 hr. Here, we present the early mixing of the $q_{v,s} < q_{\rm crit}$ test case. Mixing initiates near the top of the domain, driven by dense parcels sinking. Within the convecting layer, as compensating rising air parcels become supersaturated, water vapor condenses within them. The condensate then falls through lower cells and evaporates in subsaturated grid cells. The convecting layer moves down through the atmosphere until it reaches the surface or a neutrally stable layer. In the isothermal simulation initialized with $q_{v,s} < q_{\rm crit}$ (shown here), the convecting layer stops and stabilizes at the top of the Guillot stable region rather than reaching the surface, as in the other three isothermal simulations. After the initial rapid mixing, the isothermal simulations reach a convectively stable state, which is subsequently altered on a much slower timescale by radiative processes.

dense fluid sinks from the top of the domain (see Figure 2). However, rising plumes are saturated, and the convective stability of rising plumes is determined by the Guillot criterion. In the isothermal simulations, there is an asymmetry between the stability of rising and sinking plumes. We use CM1 simulations to understand how compositional gradients influence convective mixing, formation of layers where convection is suppressed, and the ways in which radiation can modify the temperature profile.

First, consider the isothermal test cases where the initial state $p_s = 1$ bar, $T(p) = 273$ K, and the surface $q_{v,\rm sat} \approx q_{\rm crit}$. In Figure 1, panel (a) shows the atmospheric state without the effects of radiation, while panel (b) shows the atmospheric state with radiation considered. Comparing these two rows, we find that the final vapor mixing ratio states are similar. However, there are notable differences in the upper-domain final-state temperature and relative humidity profiles.

When there are no radiative effects (panel (a) in Figure 1), temperature follows a moist adiabat from the surface up until a point in the upper atmosphere where the temperature starts to increase and becomes more isothermal. The region of the atmosphere described by the moist adiabat corresponds to a relative humidity near saturation. In the upper part of the atmosphere, the relative humidity shows the atmosphere is subsaturated. The temperature profile's shape in the upper atmosphere is similar to the observed shape of the temperature profile of noncondensing compositional convection simulations in N. Habib & R. T. Pierrehumbert (2024).

Convection is initially driven by compositionally dense air sinking from the top of the domain and heating the atmosphere adiabatically until the parcels reach the surface and can no longer sink. Simultaneously, compensating light air parcels rise and cool the atmosphere adiabatically relative to the initial state. Since the initial state was saturated, as the air parcels rise, they become supersaturated, leading to condensation and latent heat release. This process slightly warms the atmosphere, enhances mixing, and explains why the observed cooling in the upper atmosphere is not as strong as in the dry compositional convection results presented by N. Habib & R. T. Pierrehumbert (2024). Condensates, formed with $q_l > 1$ g kg^{-1}, fall through the lower atmosphere and evaporate in subsaturated grid cells, maintaining saturation in the lower atmosphere. Mixing in the lower atmosphere adjusts the temperature profile to a moist adiabat.

The final atmospheric state profiles in panel (a) of Figure 1 show the indicative atmospheric state after the initial rapid convective mixing for all four isothermal simulations, as the temperature profile will not continue to change in simulations without radiation. No liquid condensate is observed in the final state in panel (a), suggesting that all condensate formed during the initial rapid mixing phase evaporates before a stable state is reached. In the $q_{v,\rm sat} \approx q_{\rm crit}$ simulation without radiation, we find that the system rapidly adjusted due to convective mixing, and a final equilibrium state that is convectively stable is reached. Figure 2 shows snapshots of the vertical velocity, vapor mixing ratio, and condensate mixing ratio taken at five time steps *early-on* within the isothermal simulations to show how mixing occurs during the initial rapid convective adjustment phase. All four isothermal simulations experienced a similar initial rapid adjustment phase that lasted about 12–15 hr.

In the $q_{v,\mathrm{sat}} \approx q_{\mathrm{crit}}$ simulation with radiation, shown in panel (b) of Figure 1, we find the lower atmospheric temperature profile still follows a moist adiabat. However, the upper atmospheric temperature profile experiences cooling due to radiation, as it relaxes toward a radiative-equilibrium stratosphere. Radiative cooling leads to condensate formation in the upper domain after the initial rapid convective mixing phase. Note, the relative humidity in $q_{v,\mathrm{sat}} \approx q_{\mathrm{crit}}$ case with radiation remains near saturation within the entire column. Radiative cooling continuously produces condensate aloft, which subsequently evaporates and maintains near saturation in the upper domain, unlike the results in panel (a). The final state for the $q_{v,\mathrm{sat}} \approx q_{\mathrm{crit}}$ simulation with radiation is stable, with both the compositional and temperature profile stable to convection.

Panel (c) in Figure 1 shows the atmospheric state for the isothermal test case initialized with $p_s = 1$ bar and $T(p) = 300$ K, where $q_{v,s} > q_{\mathrm{crit}}$. The final atmospheric temperature profile aligns closely with a moist adiabat with the entire domain near saturation. The alignment is so perfect that the moist adiabat curve is not visible in the temperature profile plot in panel (c). Note that, for this case, the moist adiabat in a hydrogen atmosphere is itself quite close to being isothermal. The results for $q_{v,s} > q_{\mathrm{crit}}$ are similar to those where $q_{v,\mathrm{sat}} \approx q_{\mathrm{crit}}$ with radiation, but in the $q_{v,s} > q_{\mathrm{crit}}$ case, the initial rapid convective mixing is more vigorous, causing the entire domain's temperature profile to evolve to a moist adiabat. As before, after the initial mixing, condensation occurs due to radiative cooling in the upper atmosphere, forming a cloud deck in the upper domain. Overall, the system reaches a convectively stable state where both the temperature and compositional profile are stable to convection.

In the preceding cases, the Guillot criterion states that superadiabatic profiles, steeper than the moist adiabat, are stable when $q_v > q_{\mathrm{crit}}$. Given the optical thickness of the atmosphere, radiation would eventually cause the temperature profile to continue to steepen, toward the radiative-equilibrium profiles indicated in the figures. However, for optically thick atmospheres, the radiative relaxation time is long, and the steepening has not yet had time to take place to any significant extent in these simulations. The simulations provide some insight into the basic nature of radiative-convective dynamics in the compositionally stabilized regime, with the sequence consisting of a rapid adjustment to the moist adiabat followed by a much slower radiative steepening.

Panel (d) in Figure 1 shows the final isothermal CM1 test case initialized with $T = 300$ K $p_s = 20$ bar, and $q_{v,s} < q_{\mathrm{crit}}$. In this case, the initial state lower atmosphere, from the surface to $\sim 10^6$ Pa, is stable to moist convection by the Guillot criterion, but the entire atmosphere is unstable to dry convection by the Ledoux criterion. Panel (d) in Figure 1 shows a brown horizontal line dividing the initial Guillot unstable and stable regions within the atmosphere. Interestingly, no convective mixing is observed in the stable region, leaving the final state of this portion of the vertical domain in a saturated isothermal state. The upper atmosphere undergoes an initial rapid mixing phase like the preceding three isothermal simulations. However, in the $q_{v,s} < q_{\mathrm{crit}}$ case, sinking air parcels stop just below the stable boundary, and no air parcels are observed rising from the stable region. The temperature profile in the upper atmosphere follows a similar trend to the preceding isothermal simulations.

Unlike the previous three cases, in the $q_{v,s} < q_{\mathrm{crit}}$ simulation (Figure 1(d)), condensing compositional convection is stabilizing the lower domain even in the final atmospheric state. We find that moist compositional stabilization is strong enough to prevent convective mixing in the lower domain. In the lower domain, the compositional profile increases with height and is unstable according to the Ledoux criterion, but is stabilized by condensing compositional convection described by the Guillot criterion.

Since all three initially isothermal CM1 cases with radiation rapidly mixed to a moist adiabat, and thereafter only evolve slowly by radiative relaxation, we do not run the isothermal simulations further. Instead, in the next section, we initialize CM1 on the moist adiabat and run the CM1 simulation longer to better understand the radiative relaxation.

4.2. Adiabatic and Superadiabatic Simulations

Figure 3 shows an overview of the atmospheric state for the CM1 simulations initialized on the (a) dry then moist adiabat, (b) moist adiabat, and (c) superadiabatic profile. Each row shows panels that display, from left to right, vertical profiles of temperature (K), the temperature difference between the final and initial state (K), the vapor mixing ratio (kg kg^{-1}), relative humidity, and 2D cross sections taken in the middle of the y-domain of the vertical velocity (m s^{-1}) and condensate mixing ratio (g kg^{-1}). Blue lines indicates the initial state of the CM1 simulation, and the black line depicts the final state. The 2D cross sections are shown for the final state. As before, $T(p)$ and $q_v(p)$ are determined by taking the horizontal average of the 3D CM1 output at the given time step. Relative humidity is calculated using the 3D CM1 outputs for T, p, and q_v, and the horizontal average is shown. To complement the $T(p)$ and temperature difference panels in Figure 3, we provide a plot of the lapse rates in the adiabatic simulations in Figure 14 in Appendix D.

Brown dashed horizontal lines in Figure 3 are used to highlight boundaries between convective and stable atmospheric layers. The three adiabatic test cases were designed such that moist convection is inhibited according to the Guillot criterion within a region of the atmosphere where $q_v > q_{\mathrm{crit}}$. In the simulations initialized on a moist adiabat and superadiabatic state (see Figures 3(b) and (c)), the region stable against moist convection lies below the brown dashed line. In the dry then moist adiabatic simulation, shown by Figure 3(a), the layer where convection is inhibited is located in between the two brown dashed lines.

The CM1 test case initialized on a moist adiabat represents a continuation of the isothermal cases, which showed rapid mixing that led to the formation of a convectively stable state, characterized by a moist adiabat in the lower domain. The test case starting with a dry then moist adiabat reflects a more realistic scenario where the atmosphere has a deep dry convection zone below an upper moist convecting layer. Lastly, the superadiabatic case with $q_v > q_{\mathrm{crit}}$ was performed to test if saturated superadiabatic states remain stable against convection according to the Guillot criterion.

All three simulations presented in Figure 3 show condensation-driven convective inhibition. The vertical velocity panel for the moist adiabat simulation, Figure 3(b), clearly shows vertical mixing is near zero from the surface up to pressure of $\sim 2 \times 10^4$ Pa. Similarly, we observe near-zero vertical velocities in the stable region (between the two brown lines) of the dry then

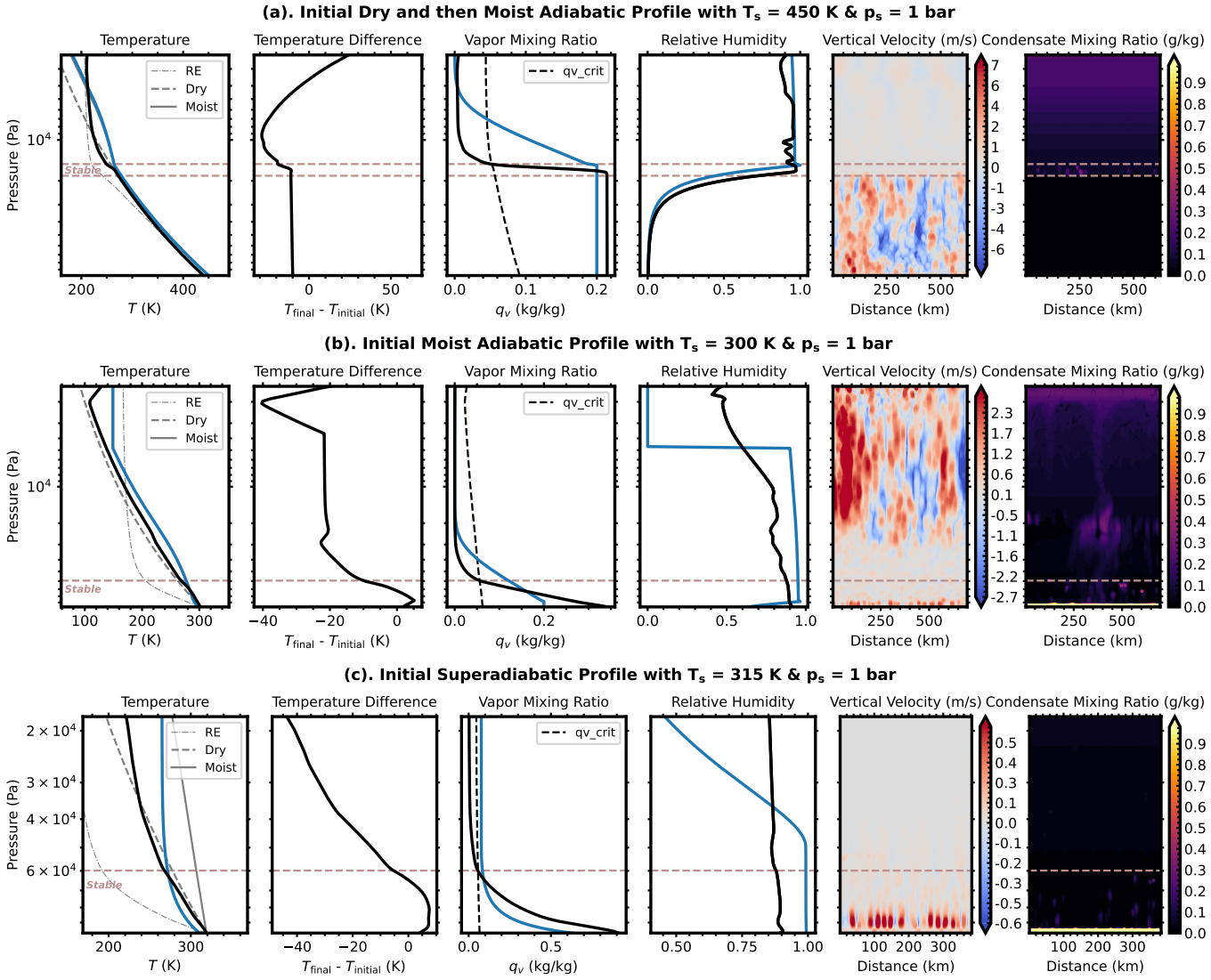

Figure 3. Atmospheric state for the CM1 simulations initialized on (a) the dry then moist adiabat, (b) the moist adiabat, and (c) the superadiabatic state. In each row, the panels show from left to right, profiles of temperature (K), the temperature difference between the final and initial state (K), the vapor mixing ratio (kg kg^{-1}), relative humidity, and vertical cross sections taken in the middle of the y-domain of vertical velocity (m s^{-1}) and condensate mixing ratio (g kg^{-1}). In the temperature panels, the gray dashed and solid lines plot dry and moist adiabats, and the gray dotted–dashed line plots the gray gas pure radiative-equilibrium temperature profile. The dashed gray line in the vapor mixing ratio panels indicates the critical vapor mixing ratio of the final state. Initial states are illustrated by blue lines in the profile plots, whereas the final state from the CM1 simulation is shown by the solid black line. The cross sections are shown for the final state. In panels (a) and (b), we observe only the initial stages of steeping toward a pure radiative-equilibrium superadiabatic state, as highlighted in the temperature difference profiles. The simulations show long radiative timescales, and the results presented here are not in a statistical-equilibrium state.

moist adiabatic test case (Figure 3(a)) and within the whole domain of the superadiabatic simulation (Figure 3(c)). The relative humidity stays near saturation in regions that are convectively stable across all three simulations in Figure 3. Further, water vapor is transported from the upper to the lower atmosphere from the initial to final state in all three simulations, as seen by in the increase in final state q_v in the lower portion of the domain. Superadiabatic temperature profiles begin to form in both Figures 3(a) and (b), but neither simulation reaches a statistical-equilibrium state. Figure 3(c) confirms that saturated superadiabatic states where $q_v > q_{\rm crit}$ remain convectively stable over time according to the Guillot criterion.

4.2.1. (a). Dry then Moist Adiabatic CM1 Simulation

Consider the CM1 simulation initialized on the dry then moist adiabat shown in Figure 3(a). The final state exhibits a three-layer structure: (i) a lower dry convective layer, (ii) a condensation-driven convective inhibition layer where vertical velocity and thus buoyancy and mixing are suppressed but the atmosphere remains near saturation, and (iii) a weak moist convective layer at the top of the domain. The brown dashed lines mark the convective inhibition layer boundaries as predicted by the Guillot criterion. The lower boundary is given by where the atmosphere first reaches saturation and $q_v(p) > q_{\rm crit}$, and the upper boundary is the level where $q_v(p) < q_{\rm crit}$, above which compositional gradients no longer inhibit convection. Interestingly, we observe that vertical velocities and convection remain suppressed above the predicted upper boundary of the convective inhibition layer (top brown dashed line; see also Figure 4).

Figure 3(a) shows the deep atmosphere approaches radiative equilibrium, as expected in regions with constant opacity and without pressure broadening. The deep atmosphere is located

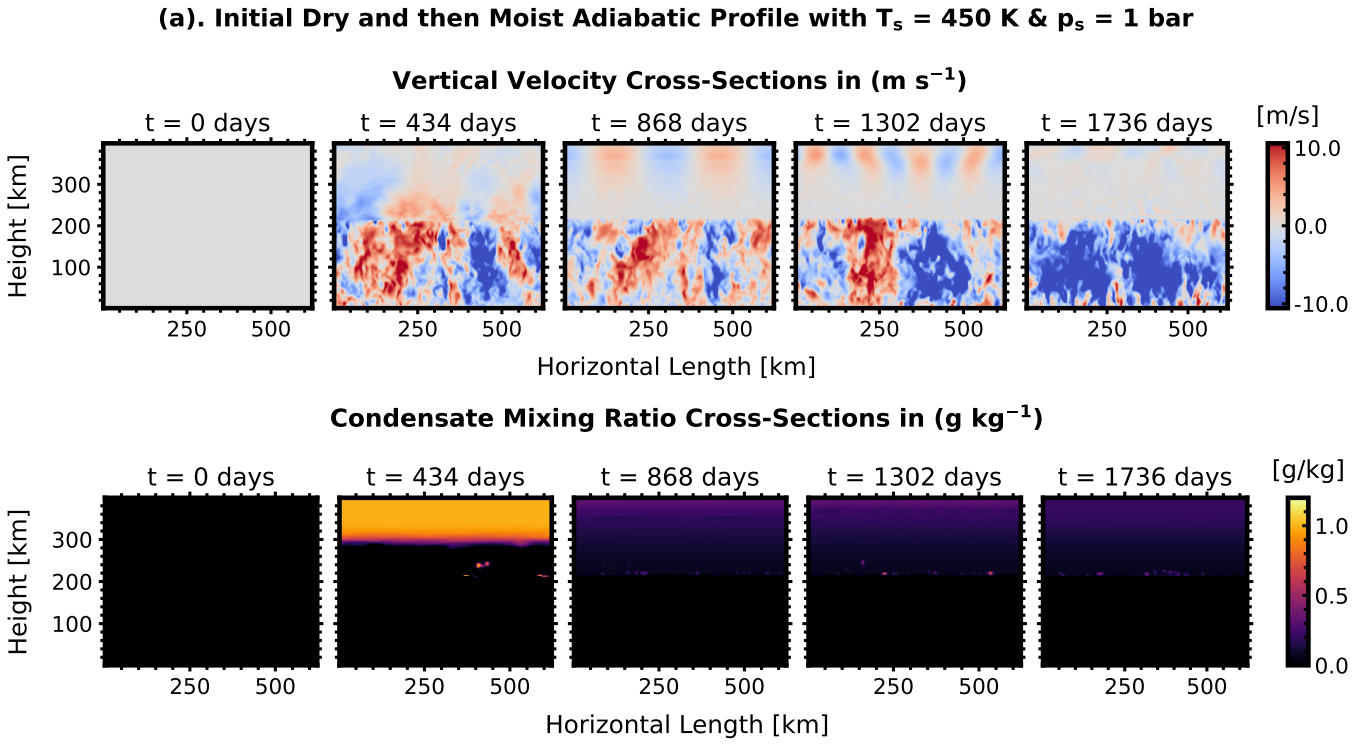

Figure 4. Vertical velocity (top row) and condensate mixing ratio (bottom row) cross sections in (x, z) taken in the middle of the y-domain for five time steps in the CM1 simulation initialized on the dry adiabat to the level of saturation from which point the initial state followed a moist adiabat. The vertical velocity cross sections show three distinct layers: a dry convective region near the surface, a layer where convection is inhibited and velocities are nearly zero, and a layer of weak moist convection in the upper atmosphere. The corresponding condensate mixing ratio plots show that a cloud deck forms in the moist convection layer, and condensates fall through and evaporate in the convective inhibition layer.

in a dry convection zone where both the vapor mixing ratio and opacity remain unchanged in our model setup. The thermal structure of the lower atmosphere is unchanged from the initial to the final state, and remains on a dry adiabat. A superadiabatic temperature structure begins to form in the stable region in between the two brown lines, as seen in the temperature difference panel in Figure 3(a). In the upper atmosphere, the temperature profile cools toward a radiative-equilibrium state leading water vapor to condense and fall through the atmosphere to the boundary of the convective inhibition layer and the dry convection layer, where it evaporates.

The water vapor mixing ratio panel in Figure 3(a) shows moisture has been transported from the upper atmosphere to the dry convection layer between the initial and final state. Further, the final state vapor mixing ratio sharply decreases in the convectively stable region, indicating reduced mixing. The relative humidity panel shows that both the convective inhibition layer and the moist convection layer in the upper atmosphere remain near saturation, suggesting that the convective stability in the stable layer should be governed by the Guillot criterion given by Equation (10).

Figure 4 shows 2D cross sections taken in the middle of the y-domain of the vertical velocities (m s^{-1}, top row) and corresponding condensate mixing ratio (g kg^{-1}, bottom row) for five time steps from the dry then moist adiabatic simulation. Figure 4 shows a distinct region where vertical mixing is suppressed separating an upper moist convection zone from a lower dry convection zone. As the simulation progresses, vertical velocities in the moist convective zone weaken due to the transport of water vapor to the dry convection zone. In the weak moist convective layer at the top of the domain, the vertical velocities are small but still greater than the convectively inhibited area.

Figures 3(a) and 4 show a cloud deck condensate with $q_l(p) < 1$ g kg^{-1} forms early in the simulation and persists within the moist convective layer. Precipitation with $q_l(p) > 1$ g kg^{-1} also develops in the moist convection layer, which then rains out and evaporates at the boundary between the stable layer and the dry convection zone. Evaporation at this boundary transports moisture to and triggers convective downdrafts in the dry convection layer. The evaporation level defines the lower boundary between the stable and dry convective layers.

To further diagnose the atmospheric layers, convective mixing, and moisture transport, Figure 5 shows the domain- and time-mean average latent and sensible heat fluxes for the dry then moist adaibat CM1 simulation. The sensible heat flux is defined by

$$Q_{\text{sensible}} = c_p \langle \rho w' T' \rangle, \tag{16}$$

and the latent heat flux is given by

$$Q_{\text{latent}} = L_v \langle \rho w' q_v' \rangle, \tag{17}$$

where c_p is the specific heat capacity at constant pressure, L_v is the latent heat of vaporization, ρ is the total atmospheric density, w' is the vertical velocity perturbation, T' is the temperature perturbation, q_v' is the vapor mixing ratio perturbation , and $\langle\rangle$ denote spatial and temporal averages. Equations (16)–(17) are calculated for the last 25 days using the vertical velocity, temperature, and mixing ratio perturbations and density output from CM1.

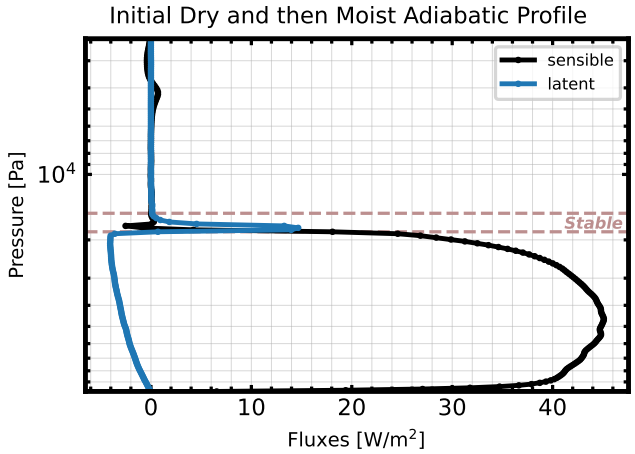

Figure 5. Domain-mean sensible and latent heat fluxes for the CM1 test case initialized on a dry then moist adiabat, averaged over the final 25 days of the simulation. The sharp drop off to zero sensible heat flux within the stable layer indicates suppressed convection. Latent heat flux dominates transport in the condensation-driven convective inhibition layer, and positive Q_{latent} values suggest upward vapor transport driven by evaporation.

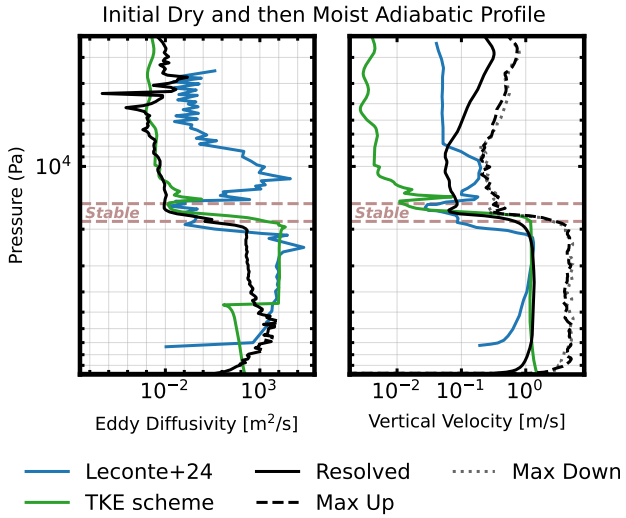

Figure 6. Eddy diffusivity (left panel) and vertical velocities (right panel) of the CM1 simulation initialized on a dry then moist adaibat. In the left panel, the eddy diffusivity from the sub-grid CM1 TKE scheme is shown in green, the resolved K_{zz}, calculated using Equation (18), is shown in black, and the eddy diffusivity from J. Leconte et al. (2024) is shown in blue. In the right panel, the rms velocity, as well as the maximum upward and maximum downward velocity from the CM1 simulation are shown in black solid, dashed, and dotted lines, respectively. The rms velocity profile from J. Leconte et al. (2024) is shown in blue for comparison. As before, the brown dashed lines mark the convectively stable region. Note, the J. Leconte et al. (2024) profile is shifted upward, such that the convective inhibition layer in their result lies within the brown dashed lines for comparative purposes.

In the dry convection layer, the sensible heat flux in Figure 5 is large and positive, indicating strong upward mixing of warm, subsaturated air in the dry convective layer. Conversely, the latent heat flux is weakly negative ($\sim$0–4 W m^{-2}), implying a net downward transport of moist air that transports moisture from the upper atmosphere to the dry convection layer, consistent with the $q_v(p)$ profile in Figure 3(a). Additionally, this weakly negative latent heat flux slightly cools the dry convection layer in agreement with the temperature profile shown in Figure 3(a).

The stable layer (between the brown dashed lines) in Figure 5 shows a sharp decline to slightly negative values ($\sim$3 W m^{-2}) in the sensible heat flux, suggesting suppressed convective mixing with weak net downward sinking of plumes, consistent with the Guillot inhibition criterion (Equation (10)). The latent heat flux in Figure 5 peaks to about 16 W m^{-2} at the base of the stable layer, indicating an upward moisture flux in the stable layer.

Above the stable layer (top brown dashed line), the sensible and latent heat fluxes remain near zero up to about 5×10^3 Pa, where small nonzero flux values suggest intermittent, shallow convective mixing, consistent with the weak moist convective layer seen in the vertical velocity panels in Figures 3(a) and 4. Overall, Figure 5 shows downward moisture transport into the dry convective layer from the upper atmosphere, and strong inhibition of mixing in the stable layer and above to about 5×10^3 Pa. Within the stable layer, the latent heat flux strongly dominates over the sensible heat flux, suggesting that some energy is carried upward by vapor transport, in agreement with J. Leconte et al. (2024). We find a latent heat flux of about 16 W m^{-2} within the convective inhibition layer, which is comparable to the $\sim$20 W m^{-2} reported by J. Leconte et al. (2024).

Lastly, to understand the impact of turbulent mixing in the 3D simulations, Figure 6 shows the eddy diffusivity flux in left panel and the rms vertical velocity profile in the right panel. The resolved eddy diffusivity, K_{zz} is defined as

$$K_{zz}^{\text{resolved}} = -\frac{\langle \rho q_v' w' \rangle}{\overline{\rho} \left\langle \frac{dq_v}{dz} \right\rangle}, \tag{18}$$

where ρ is the total atmospheric density, q_v is the vapor mixing ratio, w is the vertical velocity, z is the height, $'$ denote perturbations, and $\langle\rangle$ denote spatial and temporal averages. In Figure 6, the eddy diffusivity of the dry then moist adiabatic simulation is plotted in black, with the K_{zz} profile from J. Leconte et al. (2024) shown in blue for comparison. Additionally, we plot a green line showing the parameterized sub-grid eddy diffusivity output from CM1. CM1 uses the TKE sub-grid turbulence parameterization (adapted from J. W. Deardorff 1980), which uses a predictive TKE to determine an eddy viscosity and diffusivity to represent mixing on sub-grid scales. The TKE scheme has a stability dependence that reduces sub-grid mixing in statically stable conditions. The vertical velocity panel in Figure 6 shows the rms velocity, as well as the maximum upward and downward velocities in black solid, dashed, and dotted lines, respectively. The rms velocity profile from J. Leconte et al. (2024) is shown in blue for comparison, and the sub-grid velocity from the TKE scheme is shown in green. Note that the profiles from J. Leconte et al. (2024) are shifted so that the stable regions of the two studies align for easier comparison.

Figure 6 supports that convection is inhibited in the stable layer up to about 5×10^3 Pa. In the stable layer between the brown dashed lines, both the resolved (black line) and sub-grid TKE parameterized (green line) eddy diffusivity and rms velocities decrease by several orders of magnitude, further indicating convective inhibition. Both the rms velocity and K_{zz} only recovers weakly aloft near the top of the domain, corresponding to the weak moist convective layer. The small resolved (black line) sub-grid eddy fluxes and rms velocity suggest that moist convection at the top of the domain is driven by radiative cooling creating condensation. The resolved K_{zz}

and rms velocity do not recover or increase above the stable layer, unlike the K_{zz} profile from J. Leconte et al. (2024), which shows a strong increase in the upper atmosphere, corresponding to a dynamically driven moist convective layer. Note, J. Leconte et al. (2024) did not use or employ a sub-grid scale turbulence model; therefore, the blue profile is comparable to the resolved (black) line from our study.

Immediately above the stable layer, the TKE sub-grid K_{zz} and rms velocity do increase, suggesting sub-grid, small-scale turbulent mixing above the stable layer that transport water vapor upward. However, unlike the findings in J. Leconte et al. (2024), our results indicate that diffusive fluxes are insufficient to transport enough water vapor upward from the stable region to sustain strong moist convection.

Our model shows similar profile shape and magnitude rms vertical velocity and K_{zz} in the lower atmosphere and convective inhibition layer compared to findings in J. Leconte et al. (2024). Both the resolved K_{zz} and the rms vertical velocity remain comparable to the stable convective inhibition region above the upper boundary of the stable region, suggesting a transition or boundary layer where convection still seems to be suppressed, even though $q_v(p) < q_{\rm crit}$. The upper boundary of the stable region is defined by $q_v(p) = q_{\rm crit}$, beyond which the Guillot criterion no longer predicts convective inhibition. A transition or boundary region was not found in the results presented by J. Leconte et al. (2024).

In general, the K_{zz} and the vertical velocity profiles suggest that convection is still suppressed above the stable layer within the CM1 results, supporting earlier observations that moist convection is weakening in the upper atmosphere and the temperature profile is evolving toward radiative equilibrium. We attribute the difference in mixing magnitude above the stable layer between this work and J. Leconte et al. (2024) to variations in model setup, particularly in the condensation and turbulence parameterizations. J. Leconte et al. (2024) used a different condensation scheme and found higher latent heat fluxes than this study, which could enhance mixing in their model's upper atmosphere. Additionally, we employ a sub-grid turbulence parameterization, whereas J. Leconte et al. (2024) did not. In the TKE sub-grid parameterization used in CM1, mixing is suppressed in statically stable regions, which could further reduce mixing in the upper atmosphere in our CM1 simulation results. Due to the lower eddy diffusivity and vertical velocities in our model results, we do not transport enough water vapor upward to sustain strong moist convection in the upper atmosphere, unlike J. Leconte et al. (2024).

Overall, the dry then moist adiabatic simulation shows that condensation-driven convective inhibition layers do form in hydrogen-rich atmospheres where $q_v(p) > q_{\rm crit}$. Additionally, we find that the inhibition layer extends beyond where $q_v(p) \leqslant q_{\rm crit}$ due to a potential boundary layer and weak upward transport of water vapor. Despite the clear formation of a convective inhibition layer, we do not observe the temperature profile adjusting to a steep radiative profile. This is because the simulations were quite computationally expensive to run, and the radiative relaxation timescales are long. The dry then moist adiabatic CM1 test case confirms that convection is inhibited; thus, radiative relaxation should eventually proceed to produce steep radiative layers in the inhibited layer. In Section 4.3, we discuss and quantify the radiative relaxation timescales for all of the CM1 simulations.

4.2.2. (b). Moist Adiabatic CM1 Simulation

Generally, the moist adiabatic (b) and superadiabatic (c) CM1 simulations show trends similar to the dry then moist adiabatic simulation (a). The moist adiabatic simulation, in Figure 3(b), shows clear condensation-driven convective inhibition from the surface up to $\sim 2 \times 10^4$ Pa, where vertical velocities are near zero, and thus, buoyancy and convective mixing are suppressed. In the moist adiabatic simulation, the atmosphere has a two-layer structure: a stable convective inhibition layer from the surface to pressures nearing $\sim 2 \times 10^4$ Pa, topped by a convective layer aloft. As in the previous case, the stable layer seems to extend beyond where the Guillot criterion predicts compositionally driven convective inhibition (brown line where $q_v(p) = q_{\rm crit}$), suggesting the presence of a boundary or transition layer.

Figure 3(b) shows that the temperature profile is cooling toward radiative equilibrium within the whole domain. In the upper atmosphere, the temperature lies between a dry and moist adiabat but appears to be cooling to the radiative equilibrium, while the stable region's thermal profile is steepening over time and also evolving toward a radiative profile, as can be seen in the temperature difference plot. Moisture is transported from the upper atmosphere toward the surface between the initial and final states. A buildup of moisture at the surface is observed in the condensate mixing ratio cross section in Figure 3(b). Radiative cooling in the upper atmosphere drives condensation, which rains out and evaporates in lower grid cells, keeping the upper atmosphere at saturation and driving moist convection in the upper atmosphere. Some condensate is observed to rain out and evaporate in the inhibition layer; however, the transition boundary layer between the moist convective layer and the inhibition layer remains subsaturated.

To understand the moisture transport and convective mixing, Figure 7 shows the sensible and latent heat fluxes for the moist adiabatic simulation. The latent heat flux peaks at the surface due to enhanced evaporation-driven moisture flux from the buildup of condensates at the surface. Near the top of the stable layer, the latent heat flux peaks again, indicating upward moisture flux from the stable layer to the upper atmosphere. Above the inhibition layer, latent fluxes are small and slightly negative, suggesting a net downward transport of moist air. Conversely, the sensible heat flux is suppressed in the stable layer with weakly positive values, but shows oscillations in the upper atmosphere consistent with small-scale mixing in the upper atmosphere. The sensible heat flux remains small but does increase above the stable layer, supporting the argument for a transition layer above the stable region.

Figure 8 shows the K_{zz} (left panel) and rms vertical velocity (right panel) profiles. The black line shows the resolved K_{zz} calculated using Equation (18) in the K_{zz} panel, and rms vertical velocity in the left panel, while the green line plots the K_{zz} and vertical velocity from CM1's TKE sub-grid turbulence scheme, respectively. Within the stable layer, both the resolved and TKE-scheme eddy flux drop by 3–4 orders of magnitude (left panel), and the resolved and TKE-scheme rms vertical velocity drop by 1–2 orders of magnitude (right panel) in Figure 8, confirming strong convective inhibition and weak vertical transport across this layer. In the stable layer, the meters per second order-of-magnitude rms velocity suggest some convective mixing driven by the condensation and

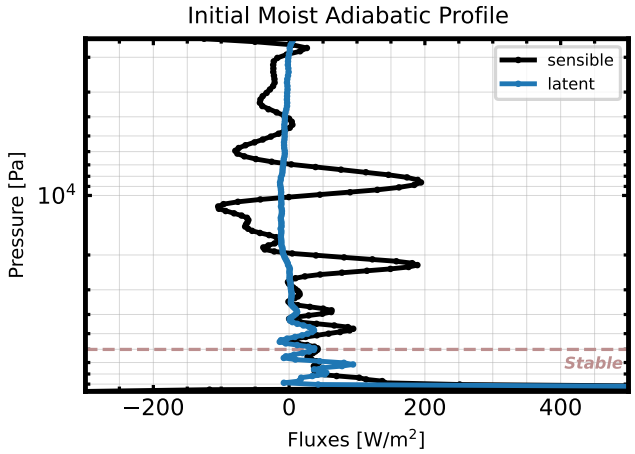

Figure 7. Domain-mean sensible and latent heat fluxes for the CM1 test case initialized on a moist adiabat calculated using Equations (16)–(17). Heat fluxes are averaged over the last 25 days of the simulation.

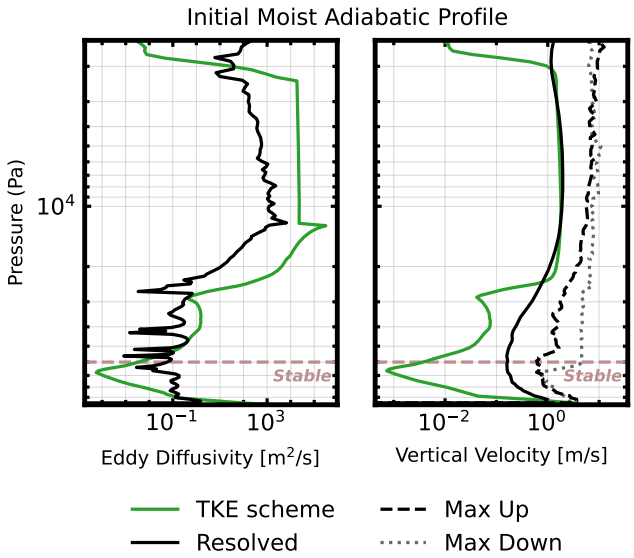

Figure 8. Eddy diffusivity (left panel) and vertical velocities (right panel) of the CM1 simulation initialized on a moist adaibat. In the left panel, the eddy diffusivity from the CM1 test case is calculated using Equation (18). In the right panel, the rms velocity, as well as maximum upward and maximum downward velocity from the CM1 simulation are shown in black solid, dashed, and dotted lines, respectively. The green line plots the eddy diffusivity and vertical velocity output from the CM1 sub-grid turbulence parameterization. As before, the brown dashed lines mark the convectively stable region.

evaporation of condensates in this layer, especially at the surface. The resolved K_{zz} and rms vertical velocity remains suppressed throughout and beyond the inhibited layer up to about 2×10^4 Pa, where they then begin to increase, consistent with weak mixing and gravity waves. Sub-grid scale mixing from the TKE parameterization increases immediately above the brown line, where the Guillot criterion predicts convective inhibition boundary, suggesting mixing is not inhibited above the convective inhibition layer but is suppressed.

As in the previous simulation, we find condensation-driven convective inhibition in the moist adiabatic simulation but do not observe a final state temperature profile on a steep radiative profile, again indicating that radiative processes are slow. Figures 7–8 suggest water vapor is transported upward at the top of the convective inhibition layer primarily by sub-grid scale turbulence, while moisture is transported from the upper atmosphere to the lower atmosphere by condensates. Over time, the upper atmosphere convection should weaken, since both the sub-grid and resolved K_{zz} fluxes are small. The moist adiabatic simulation confirms that convection is inhibited, but radiative relaxation should eventually proceed to produce steep radiative layers.

4.2.3. (c). Superadiabatic CM1 Simulation

We ran a CM1 case initialized on a saturated, superadiabatic profile to test whether superadiabatic states where $q_{v,\mathrm{sat}} \geqslant q_{\mathrm{crit}}$ remain stable over time. The superadiabatic simulation was performed, since the adiabatic and isothermal simulations discussed previously show long radiative relaxation timescales and did not converge to a superadiabatic temperature profile.

The superadiabatic simulation shows no convective mixing or significant vertical velocities throughout the entire simulation. Figure 3(c) shows the temperature profile is steepening in the full domain due to radiative cooling. In the superadiabatic simulation, the temperature profile remains superadiabatic throughout the entire simulation, but it is cooling toward the gray gas radiative-equilibrium profile.

As in previous cases, moisture is transported from the upper to lower atmosphere through condensation. Radiative cooling in the upper atmosphere produces condensates that rain out and evaporate in lower grid cells, keeping the entire atmosphere near saturation. As in the moist adiabatic case (b), condensates do build up at the surface. Vertical velocities are minimal within the full domain and primarily driven by evaporation at the surface and gravity waves.

Figure 9 shows the sensible and latent heat fluxes for the superadiabatic CM1 simulation. The latent heat flux shows a large peak at the surface due to surface-based evaporation and a smaller peak above the top of the convective inhibition layer where water vapor is being transported upward, as in the dry then moist adiabatic (a), and moist adiabatic (b) CM1 simulations. The sensible heat flux is zero in most of the domain and only peaks in correlation with the latent heat flux, indicating mixing is solely driven on small scales by condensation and evaporation in the superadiabatic simulation.

Figure 10 shows the eddy diffusivity in the left panel and rms vertical velocity in the right panel for the superadiabatic CM1 simulation. Both K_{zz} and the rms velocity are 1–2 orders of magnitude lower in the stable region compared to the dry then moist adiabatic (a), and moist adiabatic (b) CM1 simulations. As in the previous cases, above the convective inhibition layer, the sub-grid TKE scheme (green line) K_{zz} is larger than the resolved (black line) K_{zz}, suggesting upward mixing of water vapor at the boundary of the stable layer is driven by sub-grid scale turbulent mixing. Neither the K_{zz} or rms velocity recover or strongly increase above the inhibition layer, suggesting convection is suppressed in the full domain. Above the stable layer, there is a slight increase in K_{zz} and rms velocities, but generally, vertical velocities and turbulent mixing remain small throughout the domain. Near the surface, a local minimum in K_{zz}, coinciding with the lifted condensation level, could be diagnostic and does not, by itself, imply stable stratification. Assuming the latent heat flux transports the heat in the atmosphere and a vertically constant latent heat flux, K_{zz} should have a local minimum (e.g., H. Ge et al. 2024). However, Figure 9 shows a near-

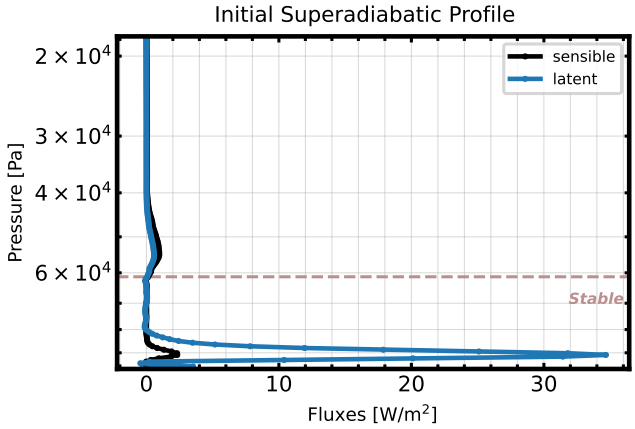

Figure 9. Domain-mean sensible and latent heat fluxes for the CM1 test case initialized on a superadiabatic profile calculated using Equations (16)–(17). Heat fluxes are averaged over the last 25 days of the simulation.

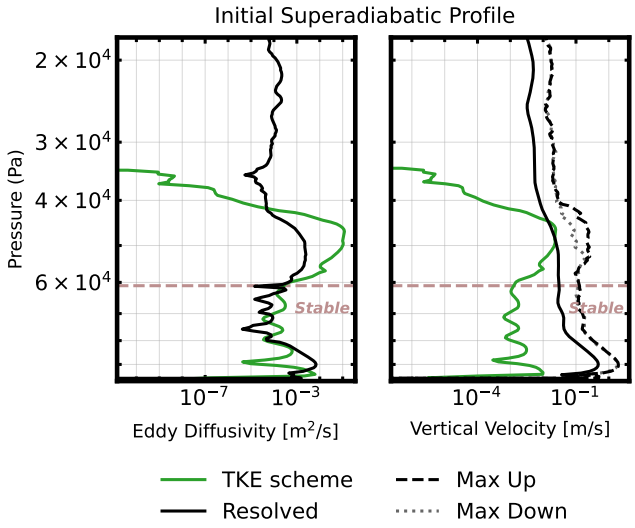

Figure 10. Eddy diffusivity (left panel) and vertical velocities (right panel) of the CM1 simulation initialized on a superadiabatic profile. In the left panel, the eddy diffusivity from the CM1 test case is calculated using Equation (18) and shown by the black line. In the right panel, the rms velocity, as well as maximum upward and maximum downward velocity from the CM1 simulation are shown in black solid, dashed, and dotted lines, respectively. The green line plots the eddy diffusivity and vertical velocity output from the CM1 sub-grid turbulence parameterization. The brown dashed lines mark the convectively stable region.

surface spike but overall suppression of latent and sensible heat fluxes, consistent with reduced turbulent mixing in this simulation.

4.3. Radiative Timescales

The radiative relaxation timescale for the CM1 simulations presented in this work is long, preventing the simulations from converging to a statistical-equilibrium state. Across the CM1 simulations, the column-mean temperature tendency is $\mathcal{O}(10^{-5}$–$10^{-7})$ K s^{-1}. At these rates, a 1 K adjustment requires roughly 1.2–116 days ($1/10^{-5} \approx 1.2$ days, $1/10^{-7} \approx 116$ days), highlighting the long radiative relaxation timescales. We estimate the radiative timescale using (i) the diffusive gray gas approximation, and (ii) a time-stepping solver that iteratively integrates the gray gas radiative transfer equations.

Table 3
Radiative Timescales for All CM1 Simulations, Estimated Using (i) the Diffusive Gray Gas Approximation (Equation (19)) and (ii) a Time-stepping Solver that Iteratively Integrates the Gray Gas Radiative Transfer Equations

	Diffusive (yr)	Time Stepping (yr)
Initial Isothermal Simulations		
(b) Isothermal $q_v \approx q_{\rm crit}$	4	4
(c) Isothermal $q_v > q_{\rm crit}$	13	1
(d) Isothermal $q_v < q_{\rm crit}$	15	4
Initial Adiabatic Simulations		
(a) Dry Then Moist Adiabat	4	1
(b) Moist Adiabat	5	5
(c) Superadiabatic	9	6

The diffusive radiative timescale required to reach gray gas radiative equilibrium is

$$t_{\rm rad} \sim \frac{p}{g}\frac{c_p}{4\sigma T^3}, \tag{19}$$

where p is the pressure, c_p is the specific heat capacity, g is the gravity, T is the temperature, and σ is the Stefan–Boltzmann constant (A. P. Showman & T. Guillot 2002). We evaluate Equation (19) for both the isothermal and adiabatic CM1 simulations using the domain- and time-mean p and T. Table 3 reports the maximum value from the profile.

Additionally, we estimate the radiative timescale by time stepping the final CM1 column toward a gray gas radiative equilibrium, defined by a height-independent net flux $F = I_+ - I_-$ (i.e., $dF/dz = 0$). The time-stepping calculation is performed in python and is initiated with the final state profiles from the CM1 simulations. Starting from the final CM1 temperature profile $T(p, 0)$, we compute upward and downward two-stream fluxes and the radiative heating rate, $\partial T/\partial t$, from the gray gas Schwarzschild equations. We then update the temperature profile by

$$T(p,\, t+1) = T(p,\, t) + \frac{dT}{dt}\cdot dt, \tag{20}$$

where $T(p, t+1)$ is the new temperature profile, $\frac{dT}{dt}$ is the calculated temperature tendency, and dt is the time step. The calculation holds the surface temperature fixed to the CM1 value (to mimic the fixed SST lower boundary condition in CM1) and keeps $q_v(p)$ and thus, $\tau(p)$ fixed in time. The new temperature profile is used to update $\partial T/\partial t$ using the gray gas radiative transfer equations. We iterate until the column maximum of $|\partial T/\partial t|$ is 2 orders of magnitude smaller than the final state CM1 heating rate. The elapsed model time provides our radiative relaxation estimate.

The time-stepping approach assumes that the atmosphere is purely radiative and neglects any further contribution from convection and dynamical feedbacks between convective and inhibited regions. Therefore, this calculation should be viewed as an indication of the time required for the inhibited regions to reach equilibrium. Table 3 reports the estimated radiative timescale from the two methods for all of the CM1 simulations. The final-state radiative fluxes and heating rates are shown in Figure 11 for the isothermal simulations (with

radiation) and Figure 12 for the adiabatic simulations in Appendix A.

5. Conclusions

Understanding the atmospheric state of planets with H_2-dominated atmospheres improves our ability to represent convection in global general circulation models and to better interpret observations of these worlds. While the simulations presented in this work focus on H_2O tracer in H_2-dominated atmospheres, convective inhibition due to condensing compositional convection is relevant for any planetary atmosphere with a condensable tracer that has a higher mean molecular weight than the background atmosphere. Examples where condensation-driven convective inhibition is important include water and ammonia in sub-Neptune exoplanets, silicates in magma-ocean planets (e.g., S. Markham et al. 2022; W. Misener & H. E. Schlichting 2022), methane and water vapor in Uranus' and Neptune's atmosphere (P. G. J. Irwin et al. 2022), and water vapor in Saturn's atmosphere (C. Li & A. P. Ingersoll 2015).

In this work, we use 3D, convection-resolving simulations to explore compositionally driven convective inhibition in H_2-dominated atmospheres. Any atmospheric tracer in a H_2-rich atmosphere is heavier than the background atmosphere. Therefore, in H_2-rich atmospheres, compositional gradients of atmospheric tracers can suppress convection, or inhibit convection if the tracer is condensing and the vapor mixing ratio exceeds a critical threshold, $q_{\rm crit}$ (T. Guillot 1995).

We test the condensation-driven convective inhibition 1D theory from T. Guillot (1995) using two sets of CM1 simulations: (i) simulations initialized on saturated isothermal profiles and (ii) simulations initialized on adiabatic profiles. The isothermal runs exhibit rapid initial convection that adjusts the column toward a moist adiabatic state where $q_v(p) > q_{\rm crit}(p)$, followed by slow radiative relaxation. The adiabatic CM1 simulations show the formation of a distinct layer where convection is inhibited, and $q_v(p) > q_{\rm crit}$. Returning to the questions posed in the introduction, we find:

1. *Is convection inhibited when the tracer abundanceis greater thanthe critical threshold defined by T. Guillot (1995)?* Both the isothermal and CM1 simulations show convective inhibition in saturated layers where $q_v(p) > q_{\rm crit}$, as evidenced by near-zero vertical velocities, reduced eddy diffusivity K_{zz}, and the sharp decline in sensible heat fluxes in the inhibited region. All three adiabatic simulations show convection remains suppressed above the inhibition layer, suggesting a transition region above the convective inhibition layer where velocities and transport of vapor remains small and suppressed.
2. *If convective inhibition regions form, is the temperature profile in these regions superadiabatic?* The temperature profile and temperature difference plots in Figures 3 suggest that the temperature profiles steepen toward radiative equilibrium within and above the inhibition layer. Generally, we find that moist convection in the upper atmosphere is driven by radiative cooling and the upper atmosphere convection weakens over time as moisture is transported to the deep atmosphere.
3. *How are heat and moisture transport impacted if convection is inhibited?* Both the isothermal and adiabatic simulations show net moisture transport, driven by condensation and rainout, from the upper to the lower atmosphere between the initial and final states. This process builds moisture in the deep atmosphere for the dry-then-moist adiabatic case, and at the surface for the other CM1 test cases. The CM1 simulations also suggest that latent heat flux and turbulent mixing do transport a small amount of water vapor and heat through the convectively inhibited layer, but it is generally too weak to sustain strong moist convection in the upper atmosphere.

A caveat of this work is that all of the simulations have relatively long radiative relaxation times, and the results have not converged to a statistical-equilibrium state. To confirm if saturated, superadiabatic temperature profiles are stable according to the Guillot criterion, we performed a CM1 simulation initialized on a saturated superadiabatic state and found it remains stable against convection throughout the simulation time. Generally, the radiation modeling setup used in this work is simplified, and we do not consider scattering, a cloud opacity or cloud-radiative feedbacks, all which should be considered in more detail in future work along with more realistic radiation schemes.

J. Leconte et al. (2024) performed a similar 3D convection-resolving simulation to determine if condensation-driven convective layers form in H_2-rich atmospheres and to characterize the resulting atmospheric state. The modeling framework and simulation setup in this work differ from those used by J. Leconte et al. (2024). J. Leconte et al. (2024) employed a correlated-k radiation scheme, did not use any sub-grid turbulence schemes, and implemented a condensation scheme where condensation occurs when $q_v(p) > q_{v,\rm sat}(p)$ and evaporation occurs at the boiling point. Conversely, in our study, we used a gray gas radiation scheme, implemented a sub-grid turbulent mixing parameterization, and used a simpler condensation scheme based on R. Rotunno & K. A. Emanuel (1987). Both studies found that convection is inhibited in saturated layers where $q_v(p) > q_{\rm crit}$ in H_2-dominated atmospheres, and that evaporation occurs at the boundary of the inhibited layer. However, in this work, we found weak water vapor transport to the upper atmosphere and weakening of the moist convective layer aloft, whereas J. Leconte et al. (2024) reported stronger upward vapor diffusion that sustains vigorous moist convection in the upper atmosphere.

Our results suggest that condensing tracers can be depleted in the upper atmosphere of planets with H_2-rich atmospheres, potentially preventing these species from being detected in sub-Neptune atmospheres. Moist convection in the upper atmosphere could be restored by a giant storm in which deep convection mixes the troposphere, as proposed by C. Li & A. P. Ingersoll (2015). After a giant storm, the tropospheric temperature profile would reset to an adiabatic state, and radiative cooling would then restart the process of cooling the atmosphere until the next storm occurs. Episodic convection in H_2-rich atmospheres has been suggested for the solar system giant planets (e.g., K. Sugiyama et al. 2011, 2014; C. Li & A. P. Ingersoll 2015; N. Clément et al. 2024; J. T. Seeley & R. D. Wordsworth 2025) and should be followed up for sub-Neptunes atmospheres.

The Guillot moist convection inhibition criterion is derived locally and assumes full saturation. Likewise, connection-resolving simulations predict local, small-scale behavior and

mixing rather than global-scale mixing or circulation. Large-scale flow, such as synoptic eddies and Hadley- or Walker-type circulations, can create subsaturation, in which case the Guillot criterion would no longer apply. Large-scale flows are not captured in convection-in-a box simulations, including our CM1 simulations. It is an interesting question of how the Guillot theory plays out in a situation when dynamic subsaturation is maintained over large regions of the atmosphere. Further, it is still unclear if superadiabatic radiative layers driven by condensation-driven convective inhibition are a planetary-wide feature. The global impact of condensation-driven convective inhibition on the mean atmospheric state and tracer transport remains to be quantified with dedicated global simulations, or at minimum, convection-resolving simulations that include the effects of large-scale circulations. For instance, how moist convection and storms that form where $q\_v(p) < q_{\rm crit}(p)$ interact with adjacent inhibited layers (e.g., via rainfall and downdrafts) is an open question (e.g., T. Guillot et al. 2022).

Further, J. Leconte et al. (2017) and A. J. Friedson & E. J. Gonzales (2017) suggested double diffusive convection should also be inhibited in the Guillot regime. We do not test double diffusive convection in the simulations presented in this work, but double diffusive convection could have an important effect on vapor transport through inhibited layers, and should be followed up in future work.

Acknowledgments

N.H. would like to thank Tristan Guillot, Steve Markham, Maxence Lefèvre, and Hamish Innes for their helpful discussions in developing this work. This research has received support from the European Research Council (ERC) under the European Union's Horizon 2020 research and innovation program (grant agreement No. 740963 to EXOCONDENSE), and from the Alfred P. Sloan Foundation under grant G202114194 to the AETHER project. The authors would like to acknowledge the use of the University of Oxford Advanced Research Computing (ARC) facility in carrying out this work. We thank the anonymous reviewer for providing suggestions that improved the final manuscript.

Appendix A
Radiative Fluxes and Temperature Tendency from the CM1 Simulations

We show an overview of the radiation fluxes and temperature tendency calculated by the TWOSTR numerical package in CM1 for the isothermal simulations in Figure 11 and the adiabatic simulations in Figure 12. In the left column , we plot the difference of the upward and downward longwave infrared flux, $I_+ - I_-$ from the respective CM1 simulation, and in the middle column, we show the temperature tendency, $\frac{dT}{dt}$, of the final state from the respective CM1 outputs. The temperature tendency is defined as

$$\frac{dT}{dt} = \frac{g}{c_{p,\rm mix}(p)} \frac{d(I_+ - I_-)}{dp}, \tag{A1}$$

where p is the pressure, T is the temperature, t is the model time, g is the gravitational acceleration, $c_{p,\rm mix}$ is the specific heat capacity at constant pressure of the mixture of background and tracer at a given pressure, and I_+ and I_- are the upward and downward longwave infrared fluxes, respectively. We find in our CM1 simulations that the temperature tendency is on the order of 10^{-5}–$10^{-7}\,\mathrm{K\,s^{-1}}$, showing that the radiative relaxation timescales are long in all of our simulations.

To quantify the radiative relaxation time, we performed a python time-stepping calculation where we estimate the time required to reach radiative equilibrium and to determine the corresponding temperature profile assuming convection is inhibited everywhere. In panel (c) of Figures 11 and 12, we plot the final temperature state from CM1 in blue, alongside the temperature profile that would result if the system were forced toward radiative equilibrium. The time-stepping calculation is described in Section 4.3. Figures 11 and 12 demonstrate that the CM1 simulation results have not yet achieved a state of statistical equilibrium, and that radiation still has the potential to modify the temperature profile, albeit over long timescales.

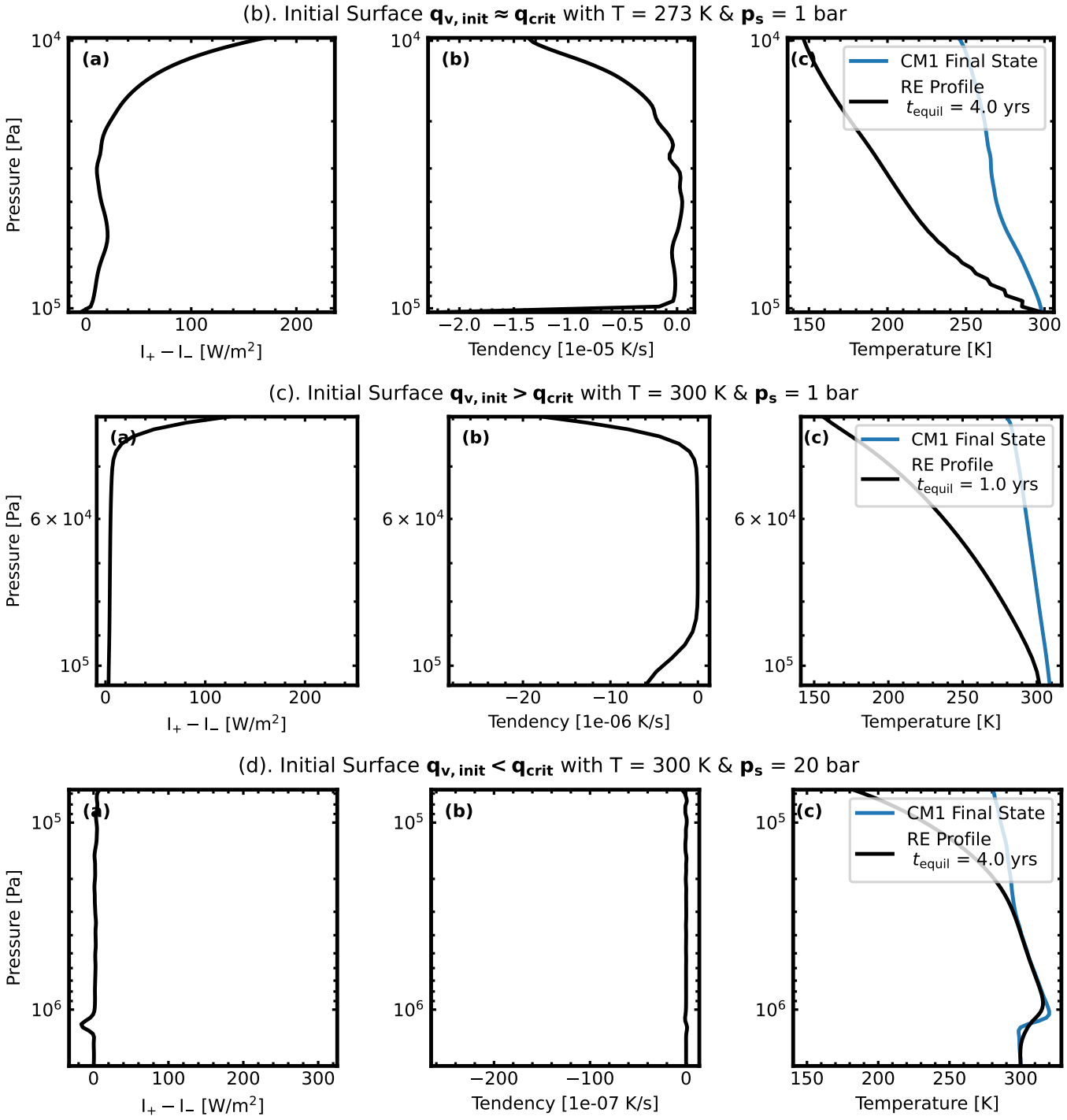

Figure 11. Radiative fluxes for the initially isothermal compositional convection CM1 simulations. Column (a) shows the difference of the upward and downward longwave infrared flux, $I_+ - I_-$, and column (b) shows the temperature tendency, $\frac{dT}{dt}$, calculated by the TWOSTR numerical package in CM1. Column (c) plots the final state CM1 profile in blue and the temperature profile from the python time-stepping calculation, which adjusts the final CM1 state toward radiative equilibrium (RE) in black.

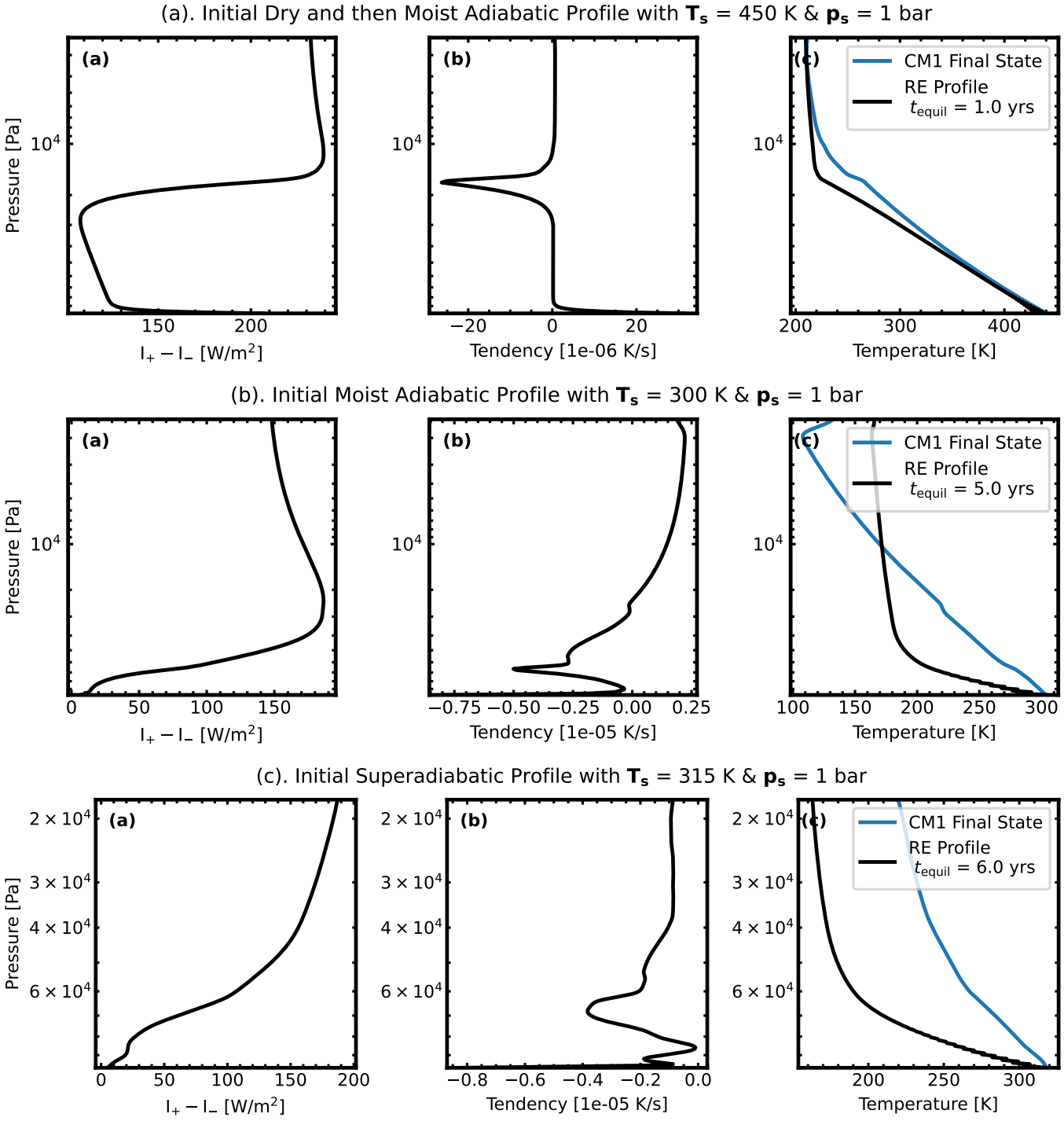

Figure 12. CM1 Radiative fluxes and estimated radiative timescale for initially adiabatic simulations. Column (a) shows the difference of the upward and downward longwave infrared flux, $I_+ - I_-$, and column (b) shows the temperature tendency, $\frac{dT}{dt}$, calculated by the TWOSTR numerical package in CM1. Column (c) plots the final state CM1 profile in blue and the temperature profile from the python time-stepping calculation, which adjusts the final CM1 state toward radiative equilibrium (RE) in black. The calculated radiative-equilibrium profile provides an indication of the radiative relaxation timescale and the temperature for the layer where convection is inhibited.

Appendix B
An Overview of the CM1 Model

The equations solved within CM1 are presented and derived in detail in P. R. Bannon (2002) and G. H. Bryan & J. M. Fritsch (2002), and are summarized within this appendix. The CM1 code and a list of publications using this model are available at https://www2.mmm.ucar.edu/people/bryan/cm1/. CM1 has been used to model pure-steam atmospheres (X. Tan et al. 2021) and cloud-convection feedback in the atmospheres of brown dwarfs (M. Lefèvre et al. 2022). The most extensive application of CM1 is the study of convective flows on Earth, covering topics such as tropical cyclones, thunderstorms, deep moist convection, and idealized studies aimed at enhancing our understanding of Earth's convection.

CM1 is a nonhydrostatic fluid flow model that is used to simulate idealized atmospheric phenomena in a 3D Cartesian

domain (x, y, z) as a function of time, t. The prognostic variables in CM1 are the 3D components of flow velocity (u, v, w), the nondimensional pressure perturbation (π'), and the potential temperature perturbation (θ'). The governing equations of CM1 are given by the ideal gas law, conservation of mass, energy, and momentum, per unit mass of the background atmosphere.

The continuity equation for an atmospheric tracer with a mass mixing ratio q_v in CM1 is given by

$$\frac{Dq_v}{Dt} = -\dot{q}_{\rm cond} - \dot{q}_{\rm dep} - \frac{1}{\rho_b}\,\nabla\cdot(\rho_v\, v_v), \tag{B1}$$

where ρ_b is the background atmosphere density, ρ_v is the atmospheric tracer density, v_v is the diffusive velocity of the atmospheric tracer (in vapor form, can be condensing or not) relative to the background atmosphere, $\dot{q}_{\rm cond}$ describes the rate at which vapor condenses to the liquid phase, $\dot{q}_{\rm dep}$ is the rate of deposition , ∇ is the del operator, and $\frac{D}{Dt}$ is the material derivative. Generally, subscript b refers to the background atmosphere while subscript v refers to the atmospheric tracer in vapor form. The last term in Equation (B1) represents the diffusion of the atmospheric tracer in vapor form relative to the background air. The diffusion term is often small and is neglected in CM1 by default. Similarly, the continuity equation applied to the density of liquid, ρ_l, and solid, ρ_s, condensate components is given by

$$\frac{Dq_l}{Dt} = \dot{q}_{\rm cond} - \dot{q}_{\rm freeze} - \frac{1}{\rho_b}\,\frac{\partial(\rho_b V_l q_l)}{\partial z}, \tag{B2}$$

$$\frac{Dq_s}{Dt} = \dot{q}_{\rm dep} + \dot{q}_{\rm freeze} - \frac{1}{\rho_b}\,\frac{\partial(\rho_b V_s q_s)}{\partial z}, \tag{B3}$$

where z is the atmospheric height, $\dot{q}_{\rm freeze}$ describes the rate at which the liquid phase freezes, $q_l = \rho_l/\rho_b$ is the mass mixing ratio of the liquid condensate, $q_s = \rho_s/\rho_b$ is the mass mixing ratio of the solid condensate, and V_s and V_l are the terminal fall velocity of the solid and liquid condensates, respectively. The condensation, deposition, and freezing rates are determined by cloud microphysics schemes.

Conservation of momentum is derived considering the gravitational force, the fluid pressure gradient, the Coriolis force, and frictional forces, which we neglect in our study but are an optional parameter that can be added within CM1. Conservation of momentum, written in terms of x, y, z components, is

$$\frac{Du}{Dt} = -\frac{1}{\rho_b(1+q_v+q_1+q_s)}\,\frac{dp}{dx} + fv, \tag{B4}$$

$$\frac{Dv}{Dt} = -\frac{1}{\rho_b(1+q_v+q_1+q_s)}\,\frac{dp}{dy} - fu, \tag{B5}$$

$$\frac{Dw}{Dt} = -\frac{1}{\rho_b(1+q_v+q_1+q_s)}\,\frac{dp}{dz} + B; \tag{B6}$$

where u, v, w are the x, y, z components of velocity, respectively, f is the Coriolis parameter given by $f = 2\Omega\sin\phi$, Ω is the rotation rate of the planet, p is the pressure, and B is the buoyancy of the air parcel. In this work, we neglect the Coriolis force and set $f = 0$. The original CM1 code calculates the buoyancy as

$$B = g\left[\frac{\theta'}{\theta_0} + (q_v - q_{v,0})\left(\frac{1}{\epsilon} - 1\right) - (q_l - q_{l,0}) - (q_s - q_{s,0})\right]. \tag{B7}$$

where θ is the potential temperature, ϵ is the mean molecular weight ratio of the tracer to the background air, and g is the gravitational acceleration. The subscript, $_0$ refers to a hydrostatic reference state, while the $'$ denotes the perturbation from the base state at a give time. However, Equation (B7) assumes dilute amounts of q_v, q_l, and q_s. We have modified the CM1 code to use a more general form of buoyancy without making the dilute approximation

$$B = -g\frac{\rho'}{\rho_0}, \tag{B8}$$

where ρ' is the total density perturbation at a given time, and ρ_0 is the total density of the reference initial state.

CM1 defines a nondimensional pressure using a reference pressure, p_{00}, as

$$\pi \equiv \left(\frac{p}{p_{00}}\right)^{\frac{R_b}{c_{p,b}}}, \tag{B9}$$

where R_b is the specific gas constant of the background atmosphere, and $c_{p,b}$ is the heat capacity at constant pressure per unit mass of the background atmosphere. Correspondingly, the potential temperature can be defined in terms of π as

$$\theta = \frac{T}{\pi}, \tag{B10}$$

where T is the temperature. The equation of state can be written in terms of π as

$$\pi = \left(\frac{\rho_b R_b \theta(1 + q_v/\epsilon)}{p_{00}}\right)^{\frac{R_b}{c_{v,b}}}, \tag{B11}$$

where $c_{v,b}$ is the heat capacity at constant volume per unit mass of the background atmosphere.

Energy conservation is expressed by equations that govern the evolution of the nondimensional pressure and potential temperature:

$$\begin{aligned}\frac{D\theta}{Dt} = &-\left(\frac{R_{\rm mix}}{c_{v,\rm mix}} - \frac{R_b\, c_{p,\rm mix}}{c_{p,b}\, c_{v,\rm mix}}\right)\theta\,\nabla\cdot\bar{u} \\ &+ \left(\frac{c_{v,b}}{c_{v,\rm mix}\, c_{p,b}\,\pi}\right)(L_v\dot{q}_{\rm cond} + L_s\dot{q}_{\rm dep} + L_f\dot{q}_{\rm freeze}) \\ &- \theta\frac{R_v}{c_{v,\rm mix}}\left(1 - \frac{R_b c_{p,\rm mix}}{c_{p,b}R_{\rm mix}}\right)(\dot{q}_{\rm cond} + \dot{q}_{\rm dep}) + \dot{q}_{\rm rad} + \dot{q}_{\rm dis}\end{aligned} \tag{B12}$$

where R_v is the gas constant of the atmospheric tracer, and $R_{\rm mix}$, $c_{v,\rm mix}$, and $c_{p,\rm mix}$ are the gas constant, specific heat capacity at constant volume, and pressure for a mixture of background air, respectively, with an atmospheric tracer given

by

$$x_{\mathrm{mix}} = x_b\left(\frac{1}{1+q_v}\right) + x_v\left(\frac{q_v}{1+q_v}\right), \tag{B13}$$

where x denotes the thermodynamic property R, c_p, or c_v, and x_{mix} can represent R_{mix}, $c_{v,\mathrm{mix}}$, or $c_{p,\mathrm{mix}}$ depending on the property. Additionally, L_v, L_s, and L_f denote the latent heat of vaporization, sublimation, and fusion, respectively. $\dot{q}_{\mathrm{rad}}$ is the potential temperature tendency due to radiation, and $\dot{q}_{\mathrm{dis}}$ is the dissipative heating rate potential temperature tendency. The mass-weighted mean velocity of the background and tracer atmospheric components, $\bar{u}$, is defined as

$$\bar{u} = \frac{\rho_b \boldsymbol{u_b} + \rho_v \boldsymbol{u_v}}{\rho_b + \rho_v}, \tag{B14}$$

where u_b is the horizontal velocity of the background atmosphere, and u_v is the horizontal velocity of the atmospheric tracer.

In CM1, pressure is determined by

$$\begin{aligned}\frac{\mathrm{D}\pi}{\mathrm{Dt}} = &-\left(\frac{R_b}{c_{p,b}}\frac{c_{p,\mathrm{mix}}}{c_{v,\mathrm{mix}}}\right)\nabla\cdot\bar{u} \\ &+ \frac{R_b}{c_{p,b}c_{v,\mathrm{mix}}\theta}\left(L_v\dot{q}_{\mathrm{cond}} + L_s\dot{q}_{\mathrm{dep}} + L_f\dot{q}_{\mathrm{freeze}}\right) \\ &- \frac{R_b}{c_{p,b}}\left(\pi\frac{R_v c_{p,\mathrm{mix}}}{R_{\mathrm{mix}}c_{v,\mathrm{mix}}}\right)\left(\dot{q}_{\mathrm{cond}} + \dot{q}_{\mathrm{dep}}\right) + \dot{q}_{\mathrm{rad}} + \dot{q}_{\mathrm{dis}}.\end{aligned} \tag{B15}$$

Equations (B15) and (B12) are used in CM1 to determine the thermodynamic state of the system.

CM1 allows for optional parameters, which include tendencies of sub-grid turbulence, additional optional diffusive tendencies, Newtonian relaxation, and cooling and warming due to condensate drag during fallout. CM1 integrates the governing equations using a third-order Runge–Kutta time differentiation and fifth-order spatial derivatives for the advection terms. The equations are evaluated in a two-step process. In the *dynamical step*, all terms involving time are integrated forward, neglecting any phase change terms. The dynamical step is followed by the *microphysical step*, where only terms involving phase changes are evaluated. CM1 then iterates between the two steps until θ converges. Once θ converges, CM1 moves onto the next time step. How the governing equations are formulated and integrated numerically is further discussed in G. H. Bryan & J. M. Fritsch (2002), G. H. Bryan (2021), and G. H. Bryan & H. Morrison (2012). The CM1 governing equations assume: the atmosphere behaves as an ideal gas, diffusive effects in the vapor phase are negligible, condensates are incompressible and have the same temperature as the surrounding background atmosphere, and all heat capacity terms are independent of temperature.

Appendix C
Dry Superadiabatic Simulation

We performed a CM1 benchmark case initialized with a dry, superadiabatic temperature profile to confirm the CM1 model behavior. The dry superadiabatic case uses the same setup as the moist superadiabatic simulation in the main text, but with moisture disabled (i.e., $q_v = 0$). As shown in Figure 13, the column adjusts to a dry adiabat, as expected. Without moisture, there is no condensation to stabilize a superadiabatic profile, so convection mixes the layer to dry-neutral stratification.

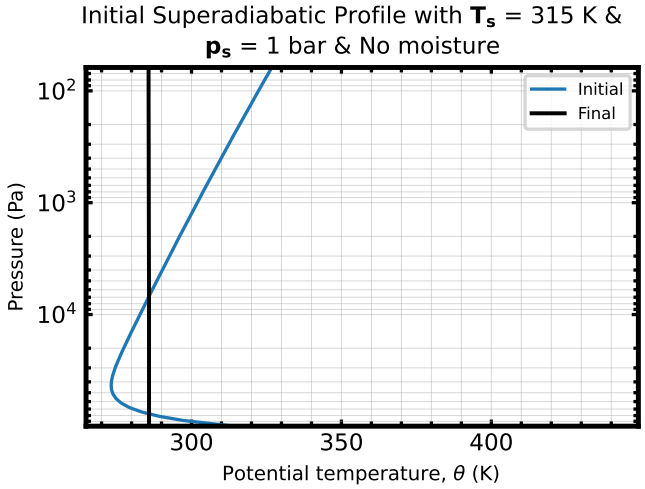

Figure 13. Potential temperature for a CM1 simulation initialized on a superadiabatic state but with no moisture, with the initial state shown by the blue line, and the final state shown by the black line. The dry superadiabat simulation was performed to benchmark the CM1 model performance.

Appendix D
CM1 Simulation Lapse Rates

As a supplement to Figures 3 and 1, Figure 14 shows the lapse rates for all six CM1 simulations with radiation. Each panel also includes reference curves for the dry-adiabatic lapse rate (gray dotted), the moist adiabatic lapse rate (blue dashed), and the gray gas radiative-equilibrium lapse rate (green dashed) for comparison.

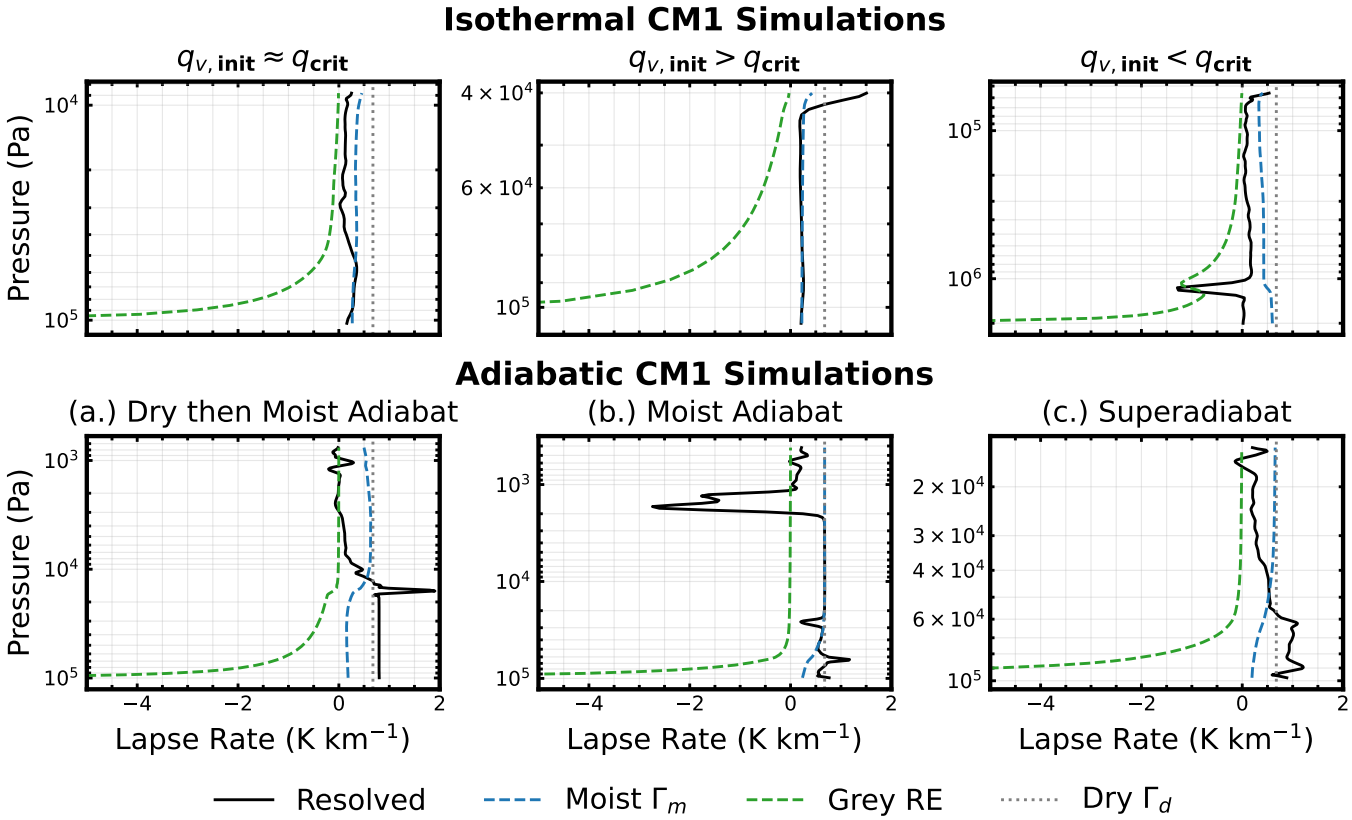

Figure 14. Lapse rates for all six CM1 simulations with radiation. In each panel, the dry-adiabatic lapse rate is shown by the gray dotted line, the moist adiabatic lapse rate is given by the blue dashed line, and the gray gas radiative-equilibrium lapse rate is shown by the green dashed line for comparison. The black line shows the lapse rate at the final time step for the respective simulation.

ORCID iDs

Namrah Habib https://orcid.org/0000-0001-7131-251X
Raymond T. Pierrehumbert https://orcid.org/0000-0002-5887-1197

References

Bannon, P. R. 2002, JAtS, 59, 1967
Benneke, B., Roy, P.-A., Coulombe, L.-P., et al. 2024, arXiv:2403.03325
Bryan, G. H. 2021, The Governing Equations for CM1 Version 10, National Center for Atmospheric Research https://www2.mmm.ucar.edu/people/bryan/cm1/cm1_equations.pdf
Bryan, G. H., & Fritsch, J. M. 2002, MWRv, 130, 2917
Bryan, G. H., & Morrison, H. 2012, MWRv, 140, 202
Clément, N., Leconte, J., Spiga, A., et al. 2024, A&A, 690, A227
Deardorff, J. W. 1980, BoLMe, 18, 495
Emanuel, K. A. 1994, Atmospheric Convection (Oxford: Oxford Univ. Press)
Freedman, R. S., Lustig-Yaeger, J., Fortney, J. J., et al. 2014, ApJS, 214, 25
Friedson, A. J., & Gonzales, E. J. 2017, Icar, 297, 160
Ge, H., Li, C., Zhang, X., & Moeckel, C. 2024, PSJ, 5, 101
Guillot, T. 1995, Sci, 269, 1697
Guillot, T., Fletcher, L. N., Helled, R., et al. 2023, in ASP Conf. Ser. 534, Protostars and Planets VII, ed. S.-i. Inutsuka et al. (San Francisco, CA: ASP), 947
Habib, N., & Pierrehumbert, R. T. 2024, ApJ, 961, 35
Innes, H., Tsai, S.-M., & Pierrehumbert, R. T. 2023, ApJ, 953, 168
Irwin, P. G. J., Teanby, N. A., Fletcher, L. N., et al. 2022, JGRE, 127, e2022JE007189
Kylling, A., Stamnes, K., & Tsay, S. C. 1995, JAtC, 21, 115
Leconte, J., Selsis, F., Hersant, F., & Guillot, T. 2017, A&A, 598, A98
Leconte, J., Spiga, A., Clément, N., et al. 2024, A&A, 686, A131
Ledoux, P. 1947, ApJ, 105, 305
Lefèvre, M., Tan, X., Lee, E. K. H., & Pierrehumbert, R. T. 2022, ApJ, 929, 153
Li, C., & Ingersoll, A. P. 2015, NatGe, 8, 398
Luque, R., & Pallé, E. 2022, Sci, 377, 1211
Madhusudhan, N., Piette, A. A. A., & Constantinou, S. 2021, ApJ, 918, 1
Markham, S., Stevenson, D., & Guillot, T. 2022, A&A, 665, A12
Menou, K. 2011, ApJL, 744, L16
Misener, W., & Schlichting, H. E. 2022, MNRAS, 514, 6025
Nicholls, H., Pierrehumbert, R. T., Lichtenberg, T., Soucasse, L., & Smeets, S. 2025, MNRAS, 536, 2957
Pierrehumbert, R. T. 2010, Principles of Planetary Climate (Cambridge: Cambridge Univ. Press)
Pierrehumbert, R. T. 2023, ApJ, 944, 20
Rotunno, R., & Emanuel, K. A. 1987, JAtS, 44, 542
Seeley, J. T., & Wordsworth, R. D. 2025, PSJ, 6, 6
Selsis, F., Leconte, J., Turbet, M., Chaverot, G., & Bolmont, É. 2023, Natur, 620, 287
Showman, A. P., & Guillot, T. 2002, A&A, 385, 166
Sugiyama, K., Nakajima, K., Odaka, M., Kuramoto, K., & Hayashi, Y. Y. 2014, Icar, 229, 71
Sugiyama, K., Nakajima, K., Odaka, M., et al. 2011, GeoRL, 38, L13201
Tan, X., Lefèvre, M., & Pierrehumbert, R. T. 2021, ApJL, 923, L15
Van Eylen, V., Agentoft, C., Lundkvist, M. S., et al. 2018, MNRAS, 479, 4786